Electronic Supporting Information

Thermally stable inorganic $Bi_{0.4}Sb_{1.6}Te_3$/metal-organic frameworks (MOFs) composites with 1-by-1 nm pore engineering towards mid-temperature thermoelectrics

Wanjia Zhang,[a] Bassem A. Al-Maythalony,[b] Fengxian Gao,[c] Fanshi Wu,[a] Wei Zhao,[a] Pengfei Xu,[a] Wenhua Zhang,[d] Cailing Chen,[e] Zhan Shi,[f] Xiyang Wang,[f] Yue Lou,*[a] and Biao Xu*[a]*

[a] School of Chemistry and Chemical Engineering, Nanjing University of Science and Technology, Nanjing 210094, China. E-mail: louyue@njust.edu.cn, xubiao@njust.edu.cn

[b] Material Discovery Research Unit, Advanced Research Center, Royal Scientific Society, Amman 11941, Jordan.

[c] School of Chemistry and Biological Engineering, University of Science and Technology Beijing, Beijing 100083, China.

[d] National Synchrotron Radiation Laboratory, Anhui Provincial Engineering Laboratory of Advanced Functional Polymer Film, University of Science and Technology of China, Hefei 230026, China.

[e] Physical Sciences and Engineering Division, Advanced Membranes and Porous Materials (AMPM) Center, King Abdullah University of Science and Technology (KAUST), Thuwal 23955-6900, Saudi Arabia.

[f] State Key Laboratory of Inorganic Synthesis and Preparative Chemistry College of Chemistry, Jilin University, Changchun 130012, China. E-mail: xiyang.wang@uwaterloo.ca

Experimental Procedures

1 Materials

2 Instrumentation and Characterizations

3 Synthesis

Results and Discussion

1 Generality for $Bi_{0.4}Sb_{1.6}Te_3$ (BST) composite ZIF-8

2 Generality for $Bi_{0.4}Sb_{1.6}Te_3$ (BST) composite UiO-66

3 Generality for $Bi_{0.4}Sb_{1.6}Te_3$ (BST) composite MIL-101

4 Generality for $Bi_{0.4}Sb_{1.6}Te_3$ (BST) composite MOF-919

5 Theoretical calculations

References for Supporting Information

Experimental Procedures

Materials. Reagents used for synthesis were: Ethylenediaminetetraacetic acid disodium salt (EDTA-2Na, AR, Nanjing Reagent), Bismuth chloride ($BiCl_3$, AR, Aladdin), Antimony trichloride ($SbCl_3$, AR, Aladdin), Tellurium powder (Te, 99.99%, Macklin), Sodium hydroxide (NaOH, 98%, Alfa Aeasar), Sodium borohydride ($NaBH_4$, AR, SCRC), Zinc nitrate hexahydrate ($Zn(NO_3)_2·6H_2O$, AR, Shanghai Chemical Reagent), 2-methylimidazole (MeIM, AR, Aladdin), Methanol (CH_3OH, AR, Macklin), Zirconium tetrachloride ($ZrCl_4$, AR, Aladdin), Terephthalic acid (H_2BDC, 99%, Aladdin), N, N-dimethylformamide (DMF, ≥99.9%, Aladdin), Chromium(III) nitrate nonahydrate ($Cr(NO_3)_3·9H_2O$, AR, Nanjing Reagent), Iron chloride hexahydrate ($FeCl_3·6H_2O$, AR, Shanghai Chemical Reagent), Copper(II) nitrate trihydrate ($Cu(NO_3)_2·3H_2O$, AR, Macklin), 1H-Pyrazole-4-carboxylic acid (H_2PyC, 98%, Bide Pharmatech), Oleylamine (OAm, 80~90%, Macklin), Oleic acid (OA, ≥99.8%, Macklin), Copper chloride (CuCl, 99.95%, Aladdin), Tin (II) chloride ($SnCl_2·2H_2O$, 99.99%, Aladdin), Selenium powder (Se, 99.99%, Macklin). All chemicals and reagents were used as received without further purification.

Instrumentation and Characterizations

Thermogravimetric analysis (TGA). TGA measurement was carried out on a thermal gravimetric analyzer (TGA 5500).

Fourier transform infrared spectroscopy (FT-IR). All FT-IR spectra of the as-prepared samples were recorded on a Thermo Nicolet iS50 spectrometer in a range of 400 - 4000 cm^{-1} at a resolution of 4 cm^{-1}.

Raman spectra. Raman spectra were obtained using a Raman microscope (Thermo Fischer DXR) with a laser at 532 nm.

Powder X-ray diffraction (PXRD). The PXRD patterns of the as-prepared samples were collected on a German Bruker D8 Advance diffractometer powder diffractometer, Cu Kα ray (λ = 1.54056 Å; 40 kV; 40 mA). The step size is 0.02°. All data were collected at ambient atmosphere and temperature.

Scanning electron microscope (SEM). The fractured surfaces for sintered samples were characterized by scanning electron microscopy (SEM, JSM-IT500HR, JEOL).

Transmission electron microscopy (TEM). Low-magnification TEM images and high-resolution TEM images were performed on an FEI Titan 80-300 microscope, operated at 300 kV.

N_2 adsorption-desorption analysis. The N_2 adsorption-desorption experiments were conducted on a Micromeritics ASAP 2460 Surface Area and Porosimetry Analyzer at 77 K by using ultra-high purity N_2. All samples were degassed at 120 °C for 10 h before the measurements.

X-ray photoelectron spectroscopy (XPS). X-ray photoelectron spectroscopy (XPS) was recorded by a PHI5000 Versa Probe system (ULVAC-PHI, Japan) with the monochromatic Al K_α line as the X-ray source.

Soft XAS and XAFS measurements. Soft XAS measurements were carried out at the beamlines of MCD-A and MCD-B (Soochow Beamline for Energy Materials) in the National Synchrotron Radiation Laboratory under vacuum conditions at room temperature. The photon energy step of N K-edge, and C K-edge XAS spectrum was set at 0.2 eV. Hard XAFS spectra of these samples are collected at the beamline of Shanghai Synchrotron Radiation Facility and the HXMA beamline of Canadian Light Source under the conditions of air atmosphere and room temperature using the transmission mode and fluorescence mode. These powders are pressed into 13 mm wafers according to the element content. These tested data are processed using the Athena and Artemis software.

Ultraviolet photo-electron spectroscopy (UPS) measurement. The ultraviolet photoelectron spectroscopy (UPS) spectra were measured on a Thermo Fisher ESCALAB Xi+ with a He I_α radiation source (hv = 21.22 eV) to determine the work functions of BST matrix and BST/0.5 wt% ZIF-8 nanocomposites.

Measurement of thermoelectric properties. The electrical conductivity and Seebeck coefficient were measured simultaneously by the static direct current method and four-probe method (CTA-3S, CRYALL). The measuring uncertainty of σ and S was ~ 5%. The thermal conductivity was calculated by $\kappa = C_p \cdot \rho \cdot D$, in which the specific heat at constant pressure (C_p) was obtained by using a differential scanning calorimetry thermalanalyzer (DSC 404 F3, NETZSCH), the pellet density (ρ) was calculated by Archimedes method and the thermal diffusivity (D) was measured using the laser flash method (Discovery Xeon Flash, TA Instrument). The measurement uncertainty of thermal conductivity κ was estimated to be within 10%, and thus the combined uncertainty for all measurements involved in zT determination is below 20%. Charge carrier concentration (p_H) and Hall mobility (μ_H) were determined from the Hall coefficient (R_H) measurement using the Van der Pauw method under a reversible magnetic field of 1.5 T (Lake Shore 8400 Series, Model 8404, USA), and from $p_H = 1/eR_H$ and $\mu_H = \sigma R_H$, respectively.

Synthesis

Synthesis of ZIF-8. In a normal procedure, $Zn(NO_3)_2 \cdot 6H_2O$ (5.58 g) was dissolved in 75 mL of methanol; then 2-methylimidazole (6.16 g) in 75 mL of methanol was subsequently injected into above solution

under vigorously stirring for 6 h at room temperature. The as-obtained precipitates were centrifuged and washed with methanol several times and dried in vacuum at 343 K for overnight.

Synthesis of UiO-66. In a typical synthesis, $ZrCl_4$ (0.175 g) and terephthalic acid (H_2BDC) (0.125 g) were dissolved in 30 mL DMF via ultrasonic treatment for 0.5 h. After that, the mixture was transferred to a Teflon-lined stainless-steel autoclave (50 mL) and heated at 120 °C for 24 h in an oven. After cooling to room temperature, the resulting white solid was separated by centrifugation, washed by DMF ultrasonic for the first time; the second time with methanol stirring washing overnight; and then ultrasonic washing with methanol for the third time. Finally, UiO-66 nanoparticles were obtained by vacuum drying for 12 h at 60 °C.

Synthesis of MIL-101 (Cr). In a typical experiment, terephthalic acid (H_2BDC) (1.66 g) and $Cr(NO_3)_3 \cdot 9H_2O$ (4.00 g) were added to deionized water (48 mL). The resulting suspension was stirred for 30 min at room temperature and then heated at 220 °C for 8 h in a Teflon-lined autoclave. After cooling to room temperature, the product was isolated from the filtrate as a green powder following centrifugation at 11000 rpm for 5 min, and then washed three times with EtOH and N, N-dimethylformamide (DMF) before drying at room temperature.

Synthesis of MOF-919-Fe. In a typical experiment, $FeCl_3 \cdot 6H_2O$ (35.5 mg), $Cu(NO_3)_2 \cdot 3H_2O$ (114.5 mg), and H_2PyC (54.0 mg) were completely dissolved in 10 mL of DMF by ultrasound in a 20 mL Pyrex vial. The mixture was heated at 100 °C for 12 h to yield green crystals after cooling to room temperature. Then, the product was isolated from the filtrate as a green powder following centrifugation at 11000 rpm for 5 min, and washed three times with EtOH and N, N-dimethylformamide (DMF) before drying at room temperature.

Synthesis of $Bi_{0.4}Sb_{1.6}Te_3$. The $Bi_{0.4}Sb_{1.6}Te_3$ nanoplates were fabricated by a facile hydrothermal method. In a typical synthetic procedure, EDTA-2Na (0.6 g), $BiCl_3$ (0.7568 g), $SbCl_3$ (2.19 g), Te powder (2.772 g) and NaOH (5 g) were dissolved in deionized water (120 mL) under vigorously stirring, followed by addition of sufficient sodium borohydride (2 g) to reduced Bi^{3+}, Sb^{3+} and Te^{2+}. The mixture was transferred to a Teflon-lined stainless-steel autoclave (200 mL) and heated at 200 °C for 12 h in an oven. The precipitate was collected by centrifugation, and then dried at 60 °C in vacuum for 12 h.

Synthesis of Cu_2SnSe_3. CuCl (1.3365 g, 13.5 mmol), $SnCl_2 \cdot 2H_2O$ (1.5230 g, 6.75 mmol), and Se poeder (1.5989 g, 20.25 mmol) were dissolved in 220 mL of OAm and 45 mL of OA. The solution was degassed at room temperature for several minutes and then purged with N_2 under magnetic stirring. Subsequently,

the solution was heated to 240 °C and maintained for 2 hours. After naturally cooling to room temperature, the products were washed with ethanol and dried under vacuum.

Fabrication of $Bi_{0.4}Sb_{1.6}Te_3$/ZIF-8, $Bi_{0.4}Sb_{1.6}Te_3$/UiO-66, $Bi_{0.4}Sb_{1.6}Te_3$/MIL-101, $Bi_{0.4}Sb_{1.6}Te_3$/MOF-919-Fe composites. ZIF-8/UiO-66/MIL-101/MOF-919-Fe powders were ultrasound dispersed into ethanol, and $Bi_{0.4}Sb_{1.6}Te_3$ powders were then added into the ZIF-8/UiO-66/MIL-101/MOF-919-Fe solution and ultrasonic together until evenly dispersed. Finally, the solution with $Bi_{0.4}Sb_{1.6}Te_3$ and ZIF-8/UiO-66/MIL-101/MOF-919-Fe was stirred magnetically for an hour and finally dried at 40 °C in vacuum for 12 h. For the preparation of bulk materials, the as-prepared powders were sintered by SPS at 673 K for ZIF-8 and UiO-66, 623 K for MIL-101, 553 K for MOF-919-Fe under pressure of 60 MPa for dwell time of 5 min in a vacuum.

Fabrication of Cu_2SnSe_3/ZIF-8. ZIF-8 powders were ultrasound dispersed into ethanol, and Cu_2SnSe_3 powders were then added into the ZIF-8 solution and ultrasonic together until evenly dispersed. Finally, the solution with Cu_2SnSe_3 and ZIF-8 was stirred magnetically for an hour and finally dried at 40 °C in vacuum for 12 h. For the preparation of bulk materials, the as-prepared powders were sintered by SPS at 673 K with an axial compressive stress of 50 MPa under vacuum and kept for 10 minutes.

Results and Discussion

Generality for $Bi_{0.4}Sb_{1.6}Te_3$ (BST) composite ZIF-8
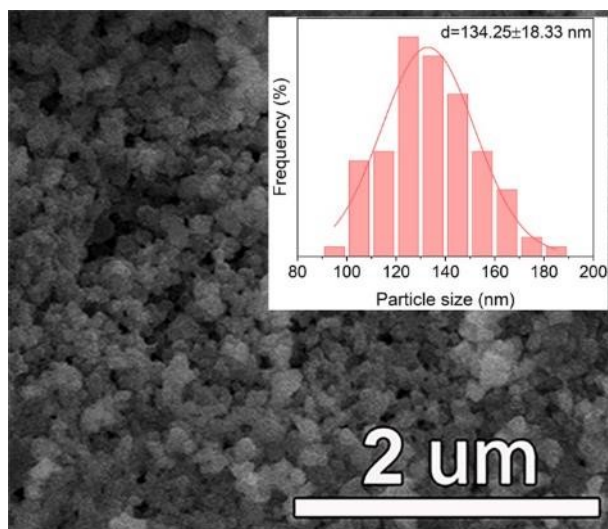

Fig. S1 SEM image of ZIF-8. This image shows that spherical particles of ZIF-8 with a diameter of 134.25 ± 18.33 nm.
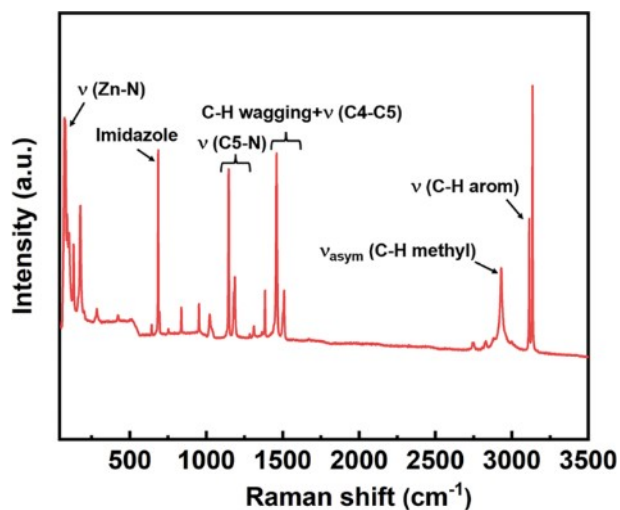

Fig. S2 Raman spectra of ZIF-8 particles. This result supports the generation of high-quality ZIF-8 particles and good agreement with previous report.[1]
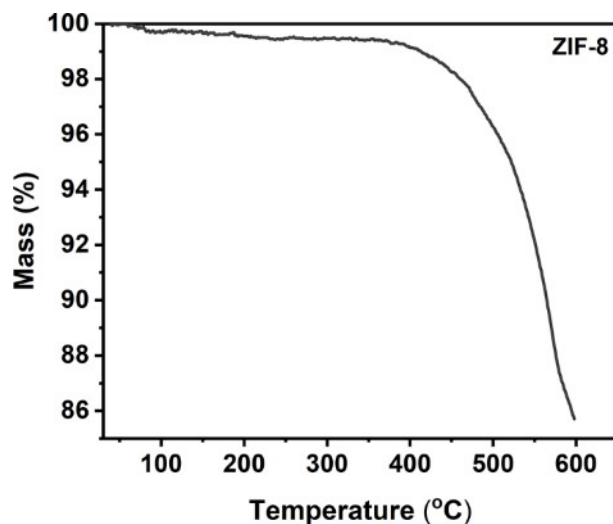
Fig. S3 TG curve for ZIF-8 measured simultaneously in a flow of N_2. The TG result indicates that the synthesized ZIF-8 is thermally stable up to 400 °C. The first weight loss, approximately 1% observed between 40 °C and 230 °C, is likely attributed to the elimination of residual DMF within the ZIF-8 cavities and/or the removal of unreacted 2-methylimidazole from the particle surface.[2] The second weight loss of about 2% at 470 °C can be attributed to the decomposition of imidazole bridges in the metal-organic framework structure of ZIF-8.[3] The third weight loss from 470 °C to 600 °C is ascribed to the decomposition and subsequent combustion of the remaining organic components in the material.[4]
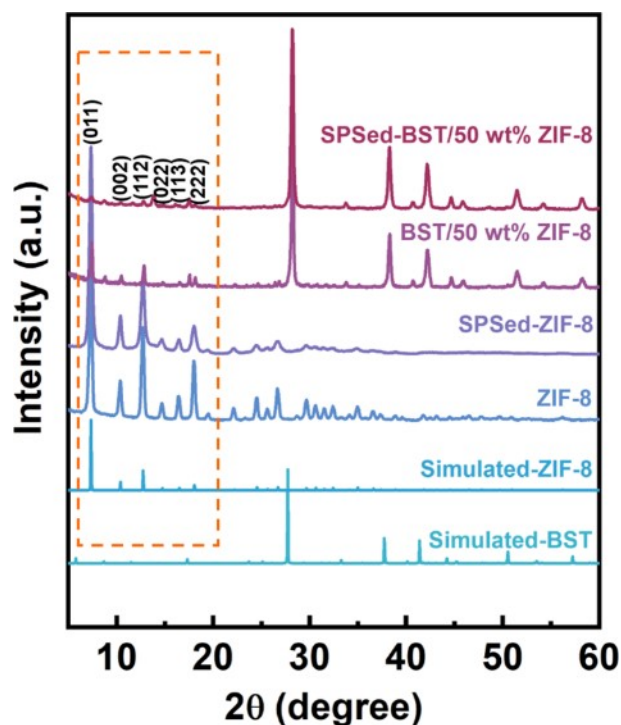
Fig. S4 Powder XRD patterns of ZIF-8, SPSed-ZIF-8, BST/50 wt% ZIF-8 and SPSed-BST/50 wt% ZIF-8. The XRD results reveal the retained ZIF-8 crystallinity (I-43m, a = 16.9910 Å) even after subjecting it to 400 °C heat treatment at

60 MPa pressure using SPS. The diffraction peaks corresponding to BST closely match the $Bi_{0.5}Sb_{1.5}Te_3$ database (PDF#49-1713). The six distinct peaks at 7.42°, 10.42°, 12.72°, 14.69°, 16.52° and 18.03° belong to the (011), (002), (112), (022), (113) and (222) planes of ZIF-8, respectively (JCPDS 00-062-1030).
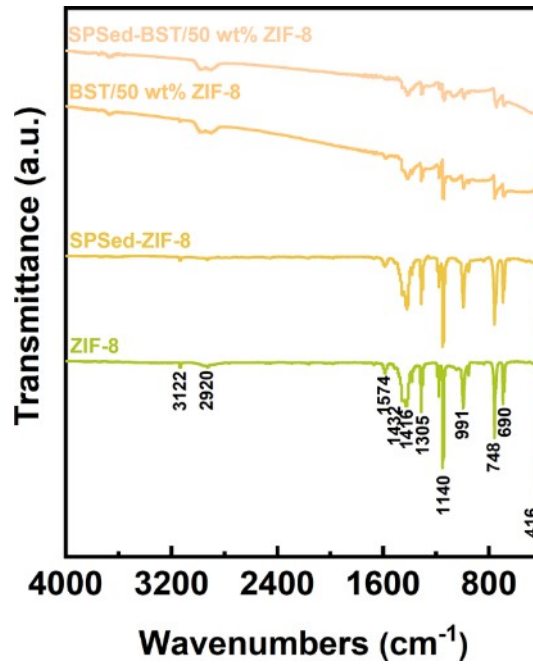

Fig. S5 The FTIR spectra of ZIF-8, SPSed-ZIF-8, BST/50 wt% ZIF-8 and SPSed-BST/50 wt% ZIF-8. The peaks at 3122 and 2920 cm^{-1} correspond to the asymmetric stretching vibrations of aliphatic C-H and aromatic rings. The absorption band at 1574 cm^{-1} is attributed to the stretching vibration of the C=N bond, and the sharp absorption band at 416 cm^{-1} results from the stretching vibration of Zn-N, indicating the binding of zinc atoms to nitrogen atoms within the 2-methylimidazolate bridges. The peaks at 1140 and 1305 cm^{-1}, 1416 and 1432 cm^{-1}, and 690 cm^{-1} correspond to the bending signals, stretching vibrations, and out-of-plane bending variation of the imidazole ring, respectively. Similarly, the peaks at 991 and 748 cm^{-1} are associated with the bending vibrations of C-N and C-H.[5-7] All the reflection peaks of ZIF-8 are present in the FTIR spectra of BST/50 wt% ZIF-8 and SPSed-BST/50 wt% ZIF-8 samples, although they are notably diminished due to the lower ZIF-8 content and the reduction in crystallinity from the sintering process.
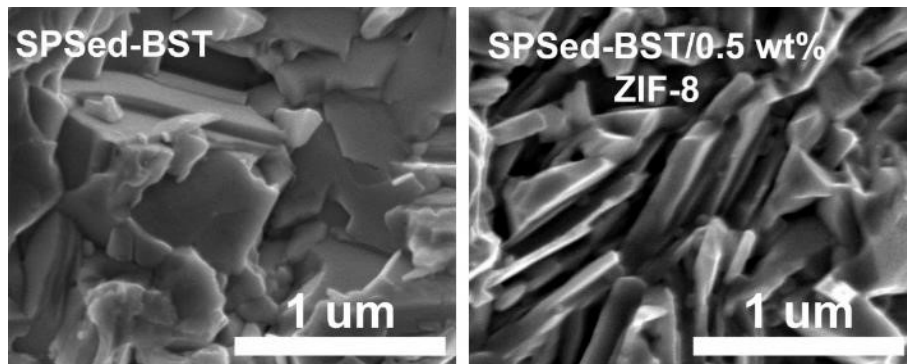

Fig. S6 SEM results. SEM images of fractured surfaces of pristine and composite samples.
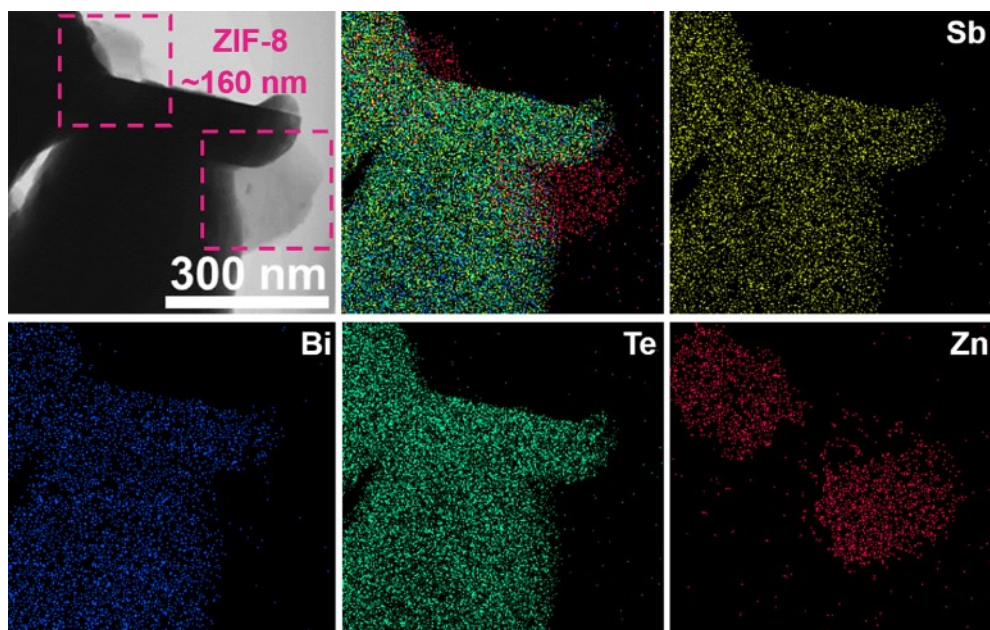
Fig. S7 EDS elemental mapping result. EDS elemental mapping images of SPSed-BST/0.7 wt% ZIF-8 demonstrate the successful introduction of ZIF-8.
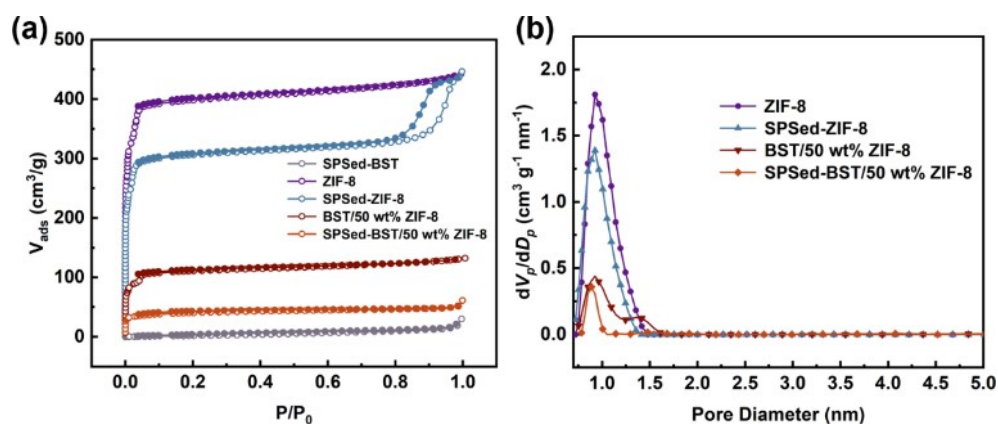

Fig. S8 (a) Nitrogen adsorption-desorption isotherms of SPSed-BST, ZIF-8, SPSed-ZIF-8, BST/50 wt% ZIF-8 and SPSed-BST/50 wt% ZIF-8. (b) Pore size distribution curves of ZIF-8, SPSed-ZIF-8, BST/50 wt% ZIF-8 and SPSed-BST/50 wt% ZIF-8.

Table S1. N_2 gas adsorption-desorption analyses of the SPSed-BST, ZIF-8, SPSed-ZIF-8, BST/50 wt% ZIF-8 and SPSed-BST/50 wt% ZIF-8.

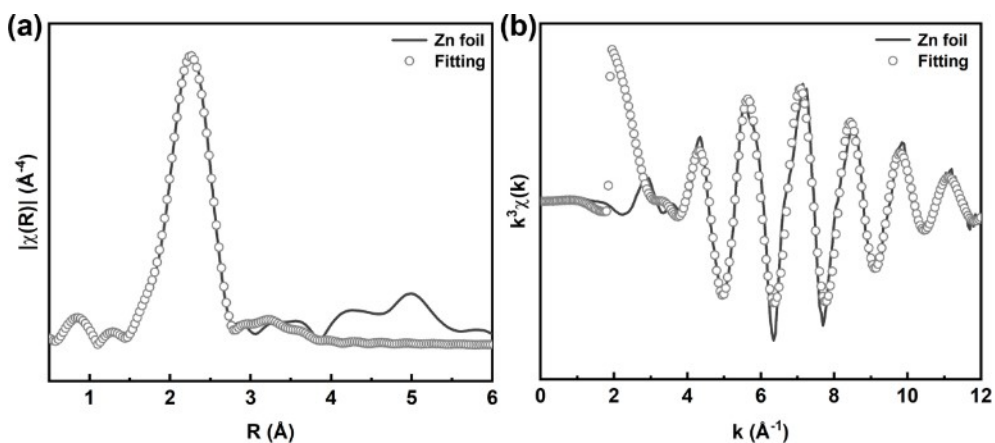| Samples	SPSed-BST	ZIF-8	SPSed-ZIF-8	BST/50 wt% ZIF-8	SPSed-BST/50 wt% ZIF-8
Surface area (m^2 g^{-1})	9.92	1718.25	1297.16	405.46	150.97

Fig. S9 (a) EXAFS *R* space fitting curve of Zn foil at Zn K-edge. (b) EXAFS *k* space fitting curve of Zn foil at Zn K-edge.
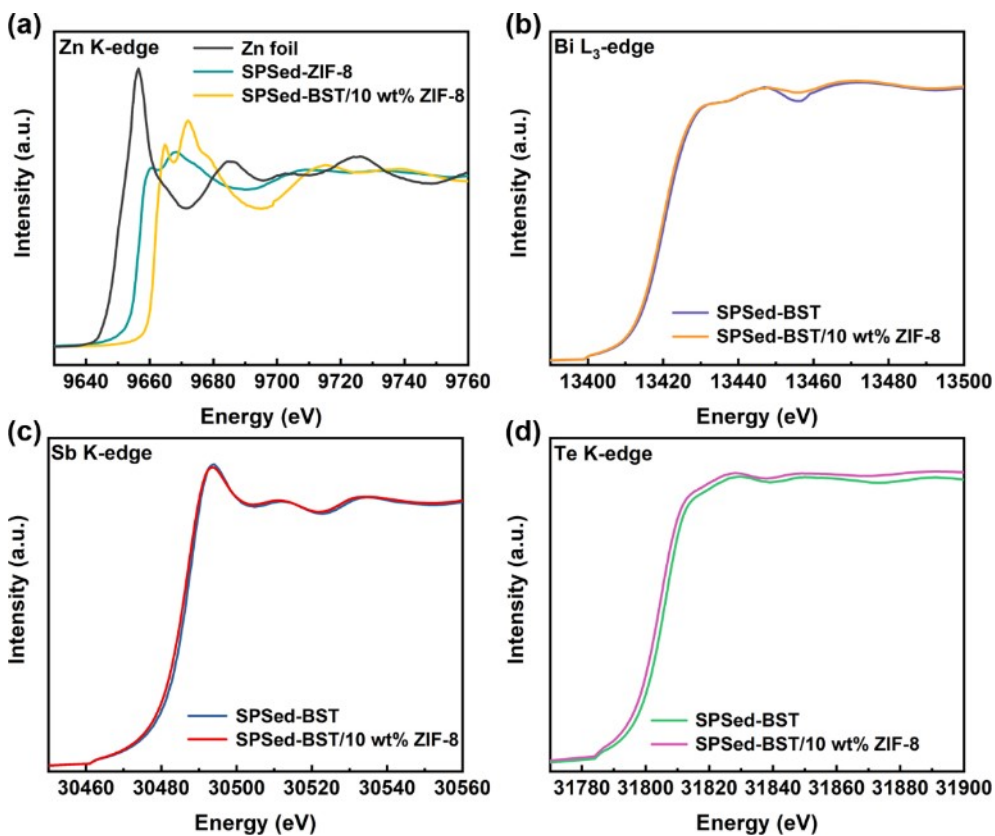

Fig. S10 (a) Zn K-edge XANES spectra of Zn foil, SPSed-ZIF-8, and SPSed-BST/10 wt% ZIF-8. (b) Bi L-edge XANES spectra of SPSed-BST and SPSed-BST/10 wt% ZIF-8. (c) Sb K-edge XANES spectra of SPSed-BST and SPSed-BST/10 wt% ZIF-8. (d) Te K-edge XANES spectra of SPSed-BST and SPSed-BST/10 wt% ZIF-8.
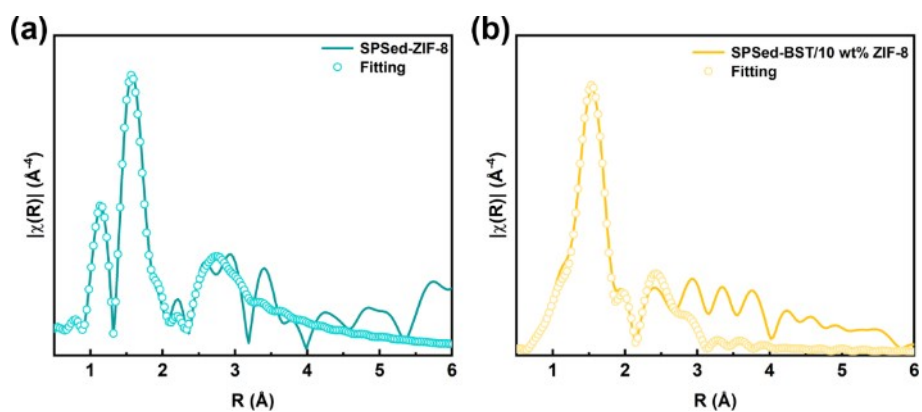
Fig. S11 EXAFS *R* space fitting curves of (a) SPSed-ZIF-8, and (b)SPSed-BST/10 wt% ZIF-8 at Zn K-edge.
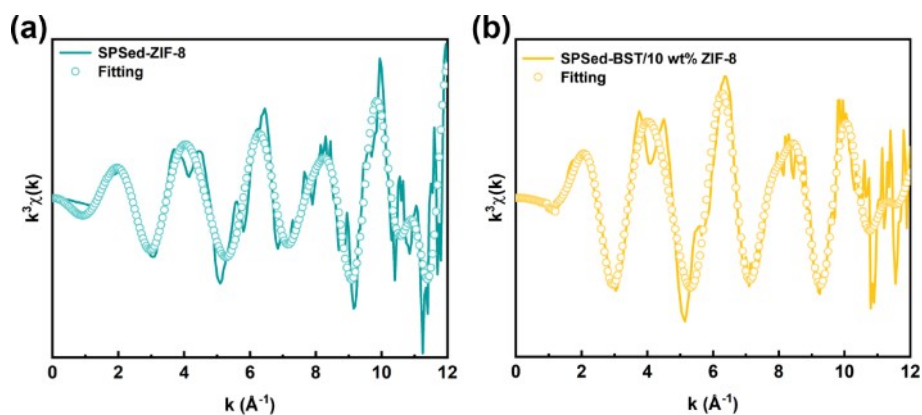

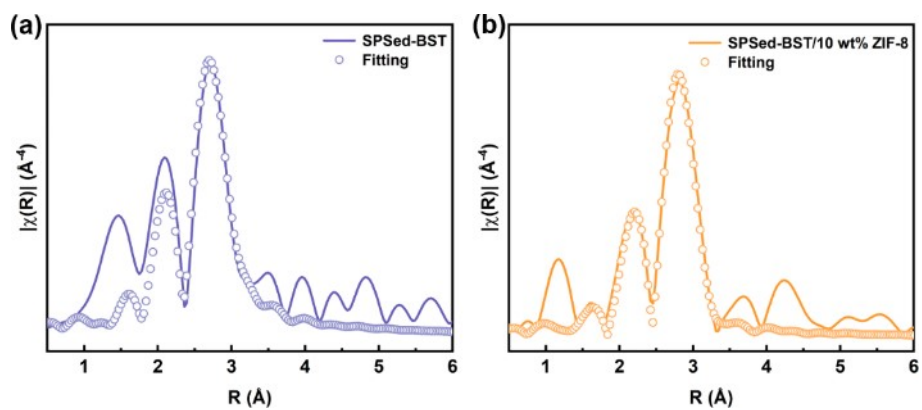**Fig. S12** EXAFS *k* space fitting curves of (a) SPSed-ZIF-8, and (b) SPSed-BST/10 wt% ZIF-8 at Zn K-edge.

Fig. S13 EXAFS *R* space fitting curve of (a) SPSed-BST, and (b) SPSed-BST/10 wt% ZIF-8 at Bi L-edge.
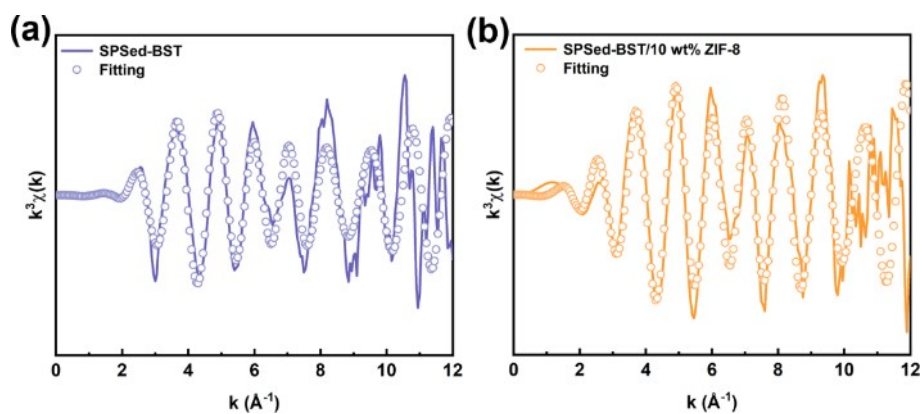
Fig. S14 EXAFS *k* space fitting curves of (a) SPSed-BST, and (b) SPSed-BST/10 wt% ZIF-8 at Bi L-edge.
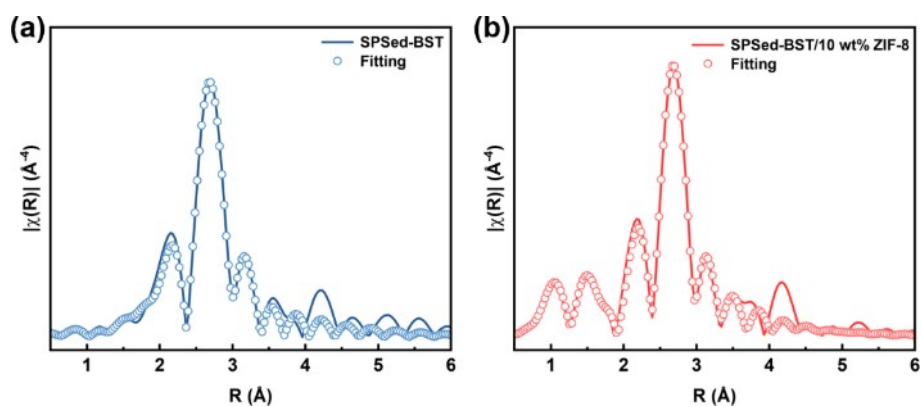

Fig. S15 EXAFS *R* space fitting curve of (a) SPSed-BST, and (b) SPSed-BST/10 wt% ZIF-8 at Sb K-edge.
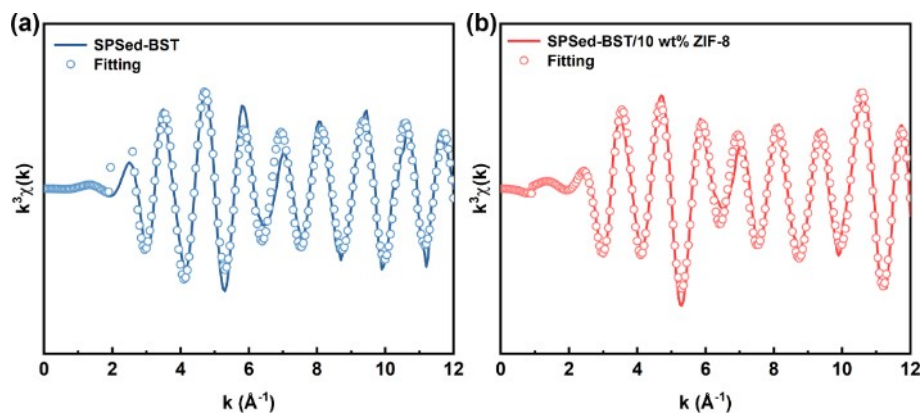

Fig. S16 EXAFS *k* space fitting curves of (a) SPSed-BST, and (b) SPSed-BST/10 wt% ZIF-8 at Sb K-edge.
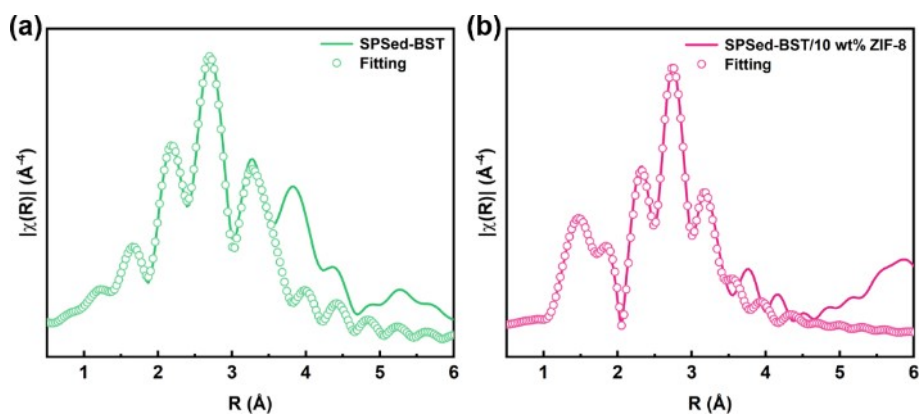
Fig. S17 EXAFS *R* space fitting curve of (a) SPSed-BST, and (b) SPSed-BST/10 wt% ZIF-8 at Te K-edge.
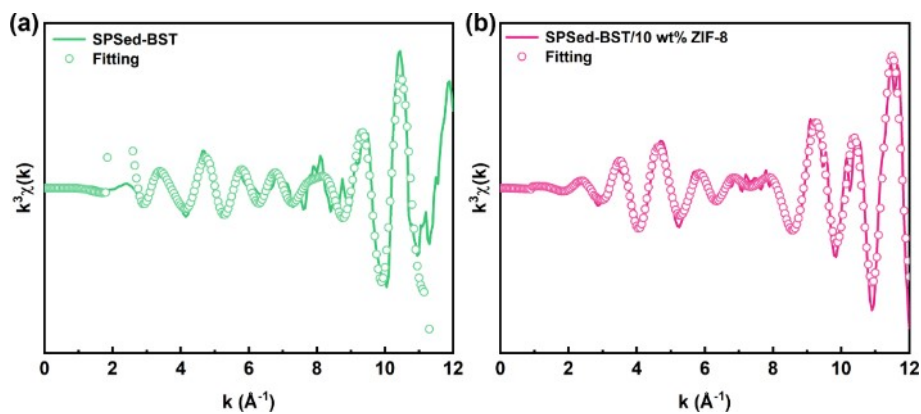

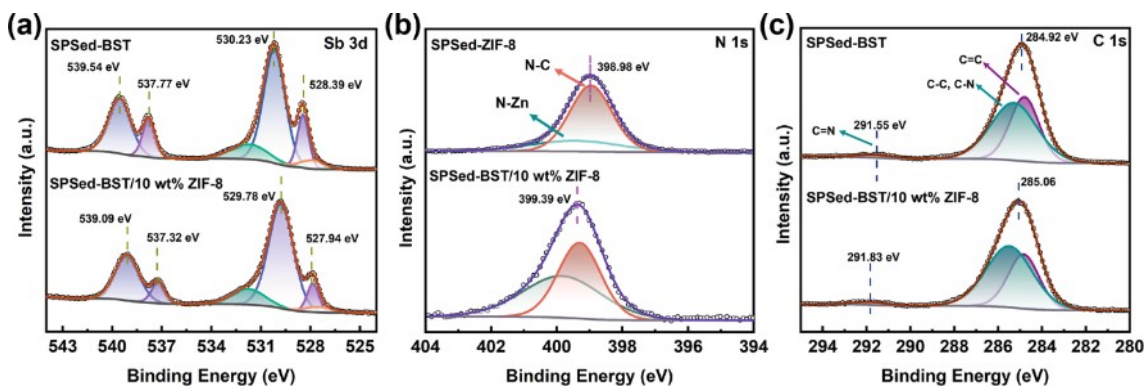**Fig. S18** EXAFS *k* space fitting curves of (a) SPSed-BST, and (b) SPSed-BST/10 wt% ZIF-8 at Te K-edge.

Fig. S19 XPS spectra of **(**a) Sb 3d, (b) N 1s, and (c) C 1s.

Table S2. EXAFS fitting parameters for the tested samples.

	Path	CN [a]	R (Å) [b]	σ^2 (10^{-3} Å²) [c]	ΔE_0 (eV) [d]	R factor (%) [e]
Zn foil	Zn-Zn	12	2.64 (0.06)	6.9 (0.5)	8.1 (0.4)	0.7
SPSed-ZIF-8	Zn-N	3.7 (0.4)	2.00 (0.04)	5.7 (0.4)	0.9 (0.2)	2
SPSed-BST	Sb-Te	2.3 (0.6)	2.94 (0.05)	7.4 (0.7)	9.8 (0.5)	3
	Sb-Te	3.7 (0.5)	3.14 (0.08)	9.7 (0.8)	3.6 (0.8)	3
	Te-Sb/Bi	6.0 (0.4)	3.03 (0.06)	3.8 (0.5)	9.3 (0.8)	0.5
SPSed-BST/10	Zn-N	4 (0.5)	1.99 (0.03)	4.3 (0.5)	5.9 (0.8)	3
wt% ZIF-8	Sb-Te	4.2 (0.8)	2.99 (0.06)	8.9 (0.7)	3.4 (0.7)	1
	Sb-Te	1.7 (0.9)	3.16 (0.07)	4.6 (0.8)	9.8 (0.4)	1
	Sb-N	1.2 (0.3)	2.06 (0.08)	9.2 (0.8)	2.4 (0.3)	1
	Te-Sb/Bi	5.8 (0.4)	3.03 (0.08)	7.6 (0.5)	3.1 (0.6)	2
	Te-N	0.7 (0.9)	2.04 (0.06)	9.8 (0.4)	0.9 (0.8)	2

a) N is the coordination number; b) R: interatomic distance between central atoms and surrounding coordination atoms; c) σ^2 is the Debye-Waller factor to measure thermal and static disorder in absorber-scatter distances; d) ΔE_0: edge-energy shift (the difference between the zero kinetic energy value of the sample and that of the theoretical model); e) R factor is used to value the goodness of the fitting. The number in the bracket is the error.

Table S3. The density of the SPS sintered BST/ZIF-8 nanocomposite.

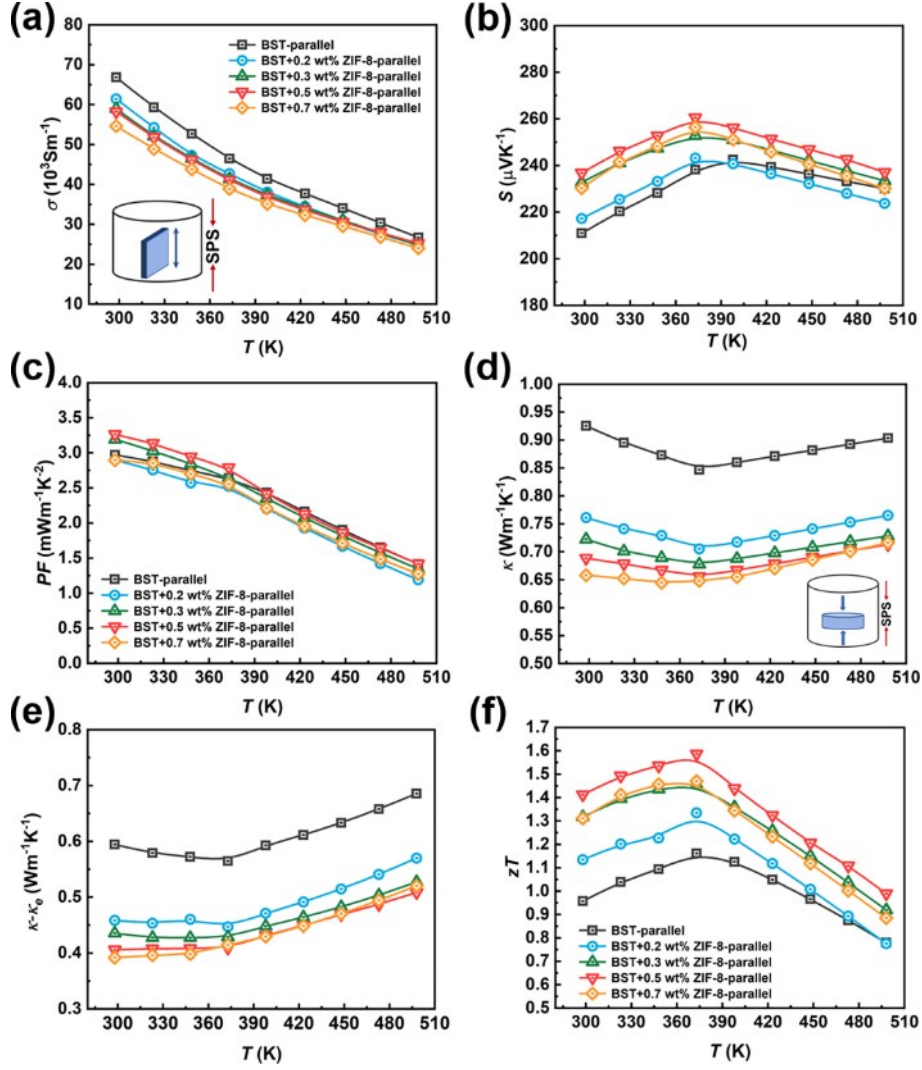| Samples	BST	BST/0.2 wt% ZIF-8	BST/0.3 wt% ZIF-8	BST/0.5 wt% ZIF-8	BST/0.7 wt% ZIF-8
Density (g/cm³)	6.62	6.57	6.49	6.39	6.30
Relative Density	98.3%	97.5%	96.3%	94.9%	93.5%

Fig. S20 Temperature-dependent thermoelectric properties of BST/x wt% ZIF-8 samples measured in the direction parallel to SPS compressing. (a) Electrical conductivity σ. (b) Seebeck coefficient S. (c) Power factor PF. (d) Total thermal conductivity κ_{tot}. (e) κ_{tot}-κ_e term. (f) Figure of merit zT.
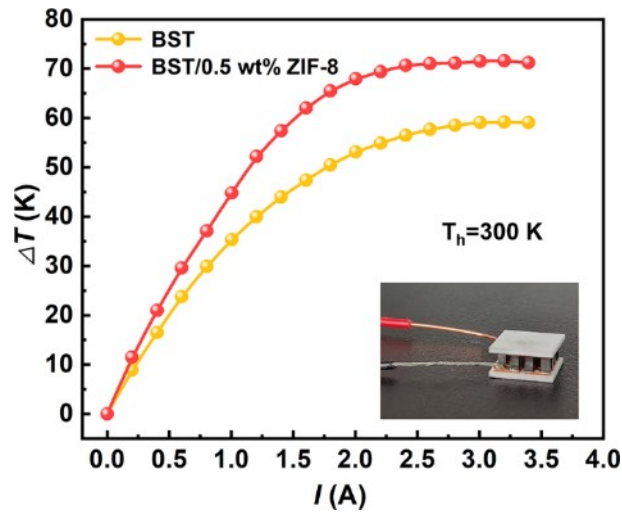
Fig. S21 The electrical current dependence of the measured cooling performance (*ΔT*, temperature drop from initial temperature) for the seven-pair thermoelectric cooling module. The hot side temperature is 300 K.
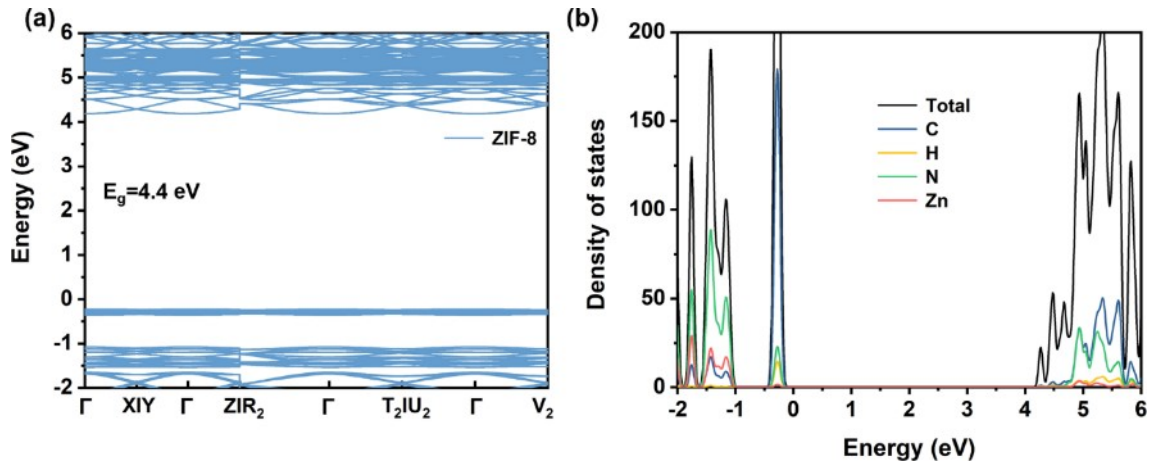
Fig. S22 (a) Electronic band structure and (b) density of states (DOS) of ZIF-8.
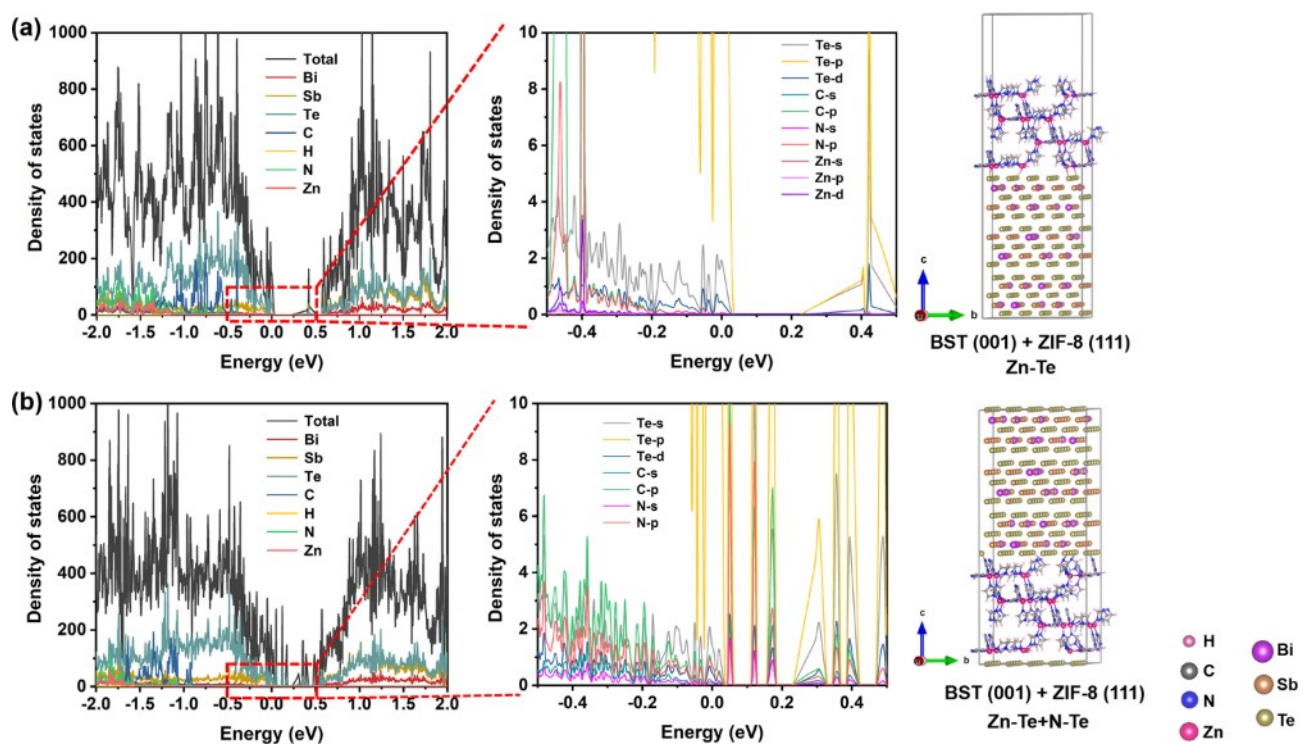
Fig. S23 Electronic density of states (DOS) of (a) BST (001) + ZIF-8 (111) with Zn-Te bonding and (b) BST (001) + ZIF-8 (111) with Zn-Te and N-Te bonding.

Fig. S24a demonstrates a decrease in electrical conductivity (σ) with the increase in ZIF-8 content. This phenomenon is attributed to the augmented interface density and carrier scattering induced by sub-nanopores. The Cu_2SnSe_3/ZIF-8 samples exhibit notably enhanced Seebeck coefficient (S) values in comparison to the Cu_2SnSe_3 matrix (Fig. S24b). This enhancement compensates for the degradation of electrical conductivity and improves the power factor (PF) (Fig. S24c). Moreover, the introduction of ZIF-8 second phase and sub-nanopore structure leads to a substantial reduction in thermal conductivity (κ) (Fig. S24d). Consequently, the zT values of the Cu_2SnSe_3/x wt% ZIF-8 composites outperform those of the pure Cu_2SnSe_3 (Fig. S24f) due to the improved S and significantly reduced κ, demonstrating the well applicability and universality of our work.
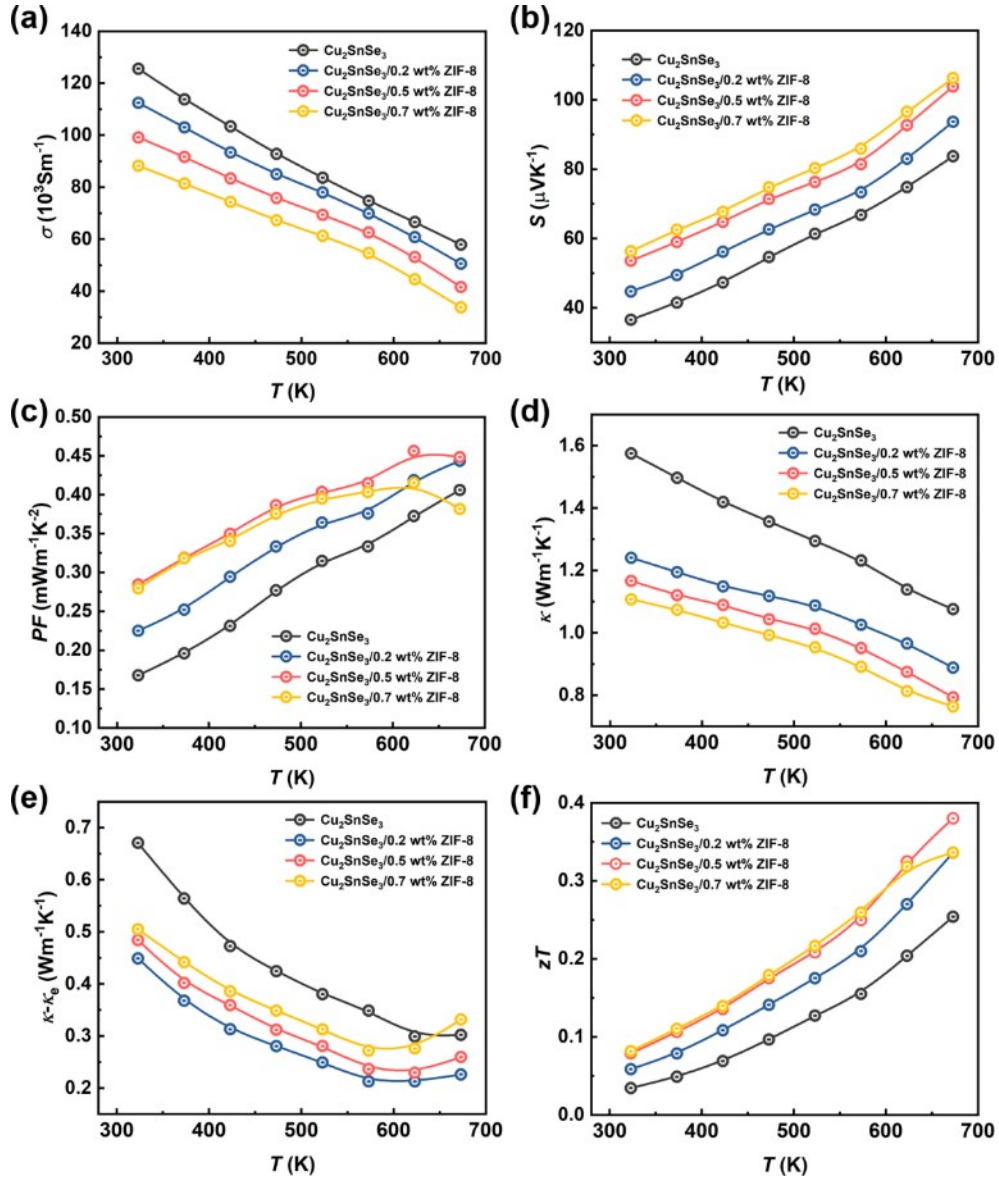
Fig. S24 Temperature-dependent thermoelectric properties of Cu_2SnSe_3/x wt% ZIF-8 (x = 0, 0.2, 0.5, 0.7) samples. (a) Electrical conductivity σ. (b) Seebeck coefficient S. (c) Power factor PF. (d) Total thermal conductivity κ_{tot}. (e) κ_{tot}-κ_e term. (f) Figure of merit zT.
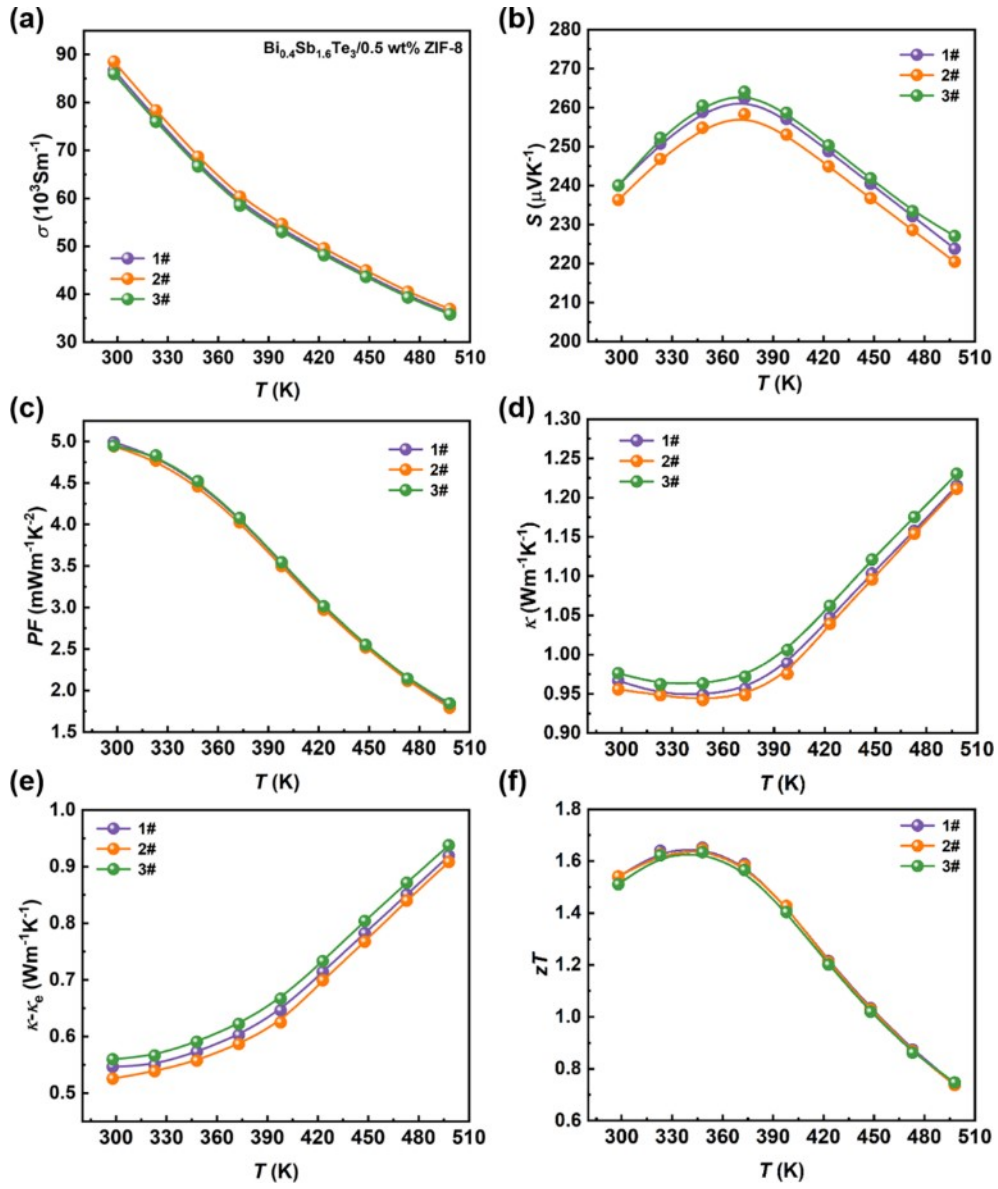
Fig. S25 Data repeatability of temperature-dependent thermoelectric properties (a) electrical conductivity σ, (b) Seebeck coefficient S, (c) power factor PF, (d) total thermal conductivity κ_{tot}, (e) κ_{tot}-κ_e term, and (f) figure of merit zT for $Bi_{0.4}Sb_{1.6}Te_3$/0.5 wt% ZIF-8 sample.

Fig. S26 Data cyclic stability of temperature-dependent thermoelectric properties (a) electrical conductivity σ, (b) Seebeck coefficient S, (c) power factor PF, (d) total thermal conductivity κ_{tot}, (e) κ_{tot}-κ_e term, and (f) figure of merit zT for $Bi_{0.4}Sb_{1.6}Te_3$/0.5 wt% ZIF-8 sample.


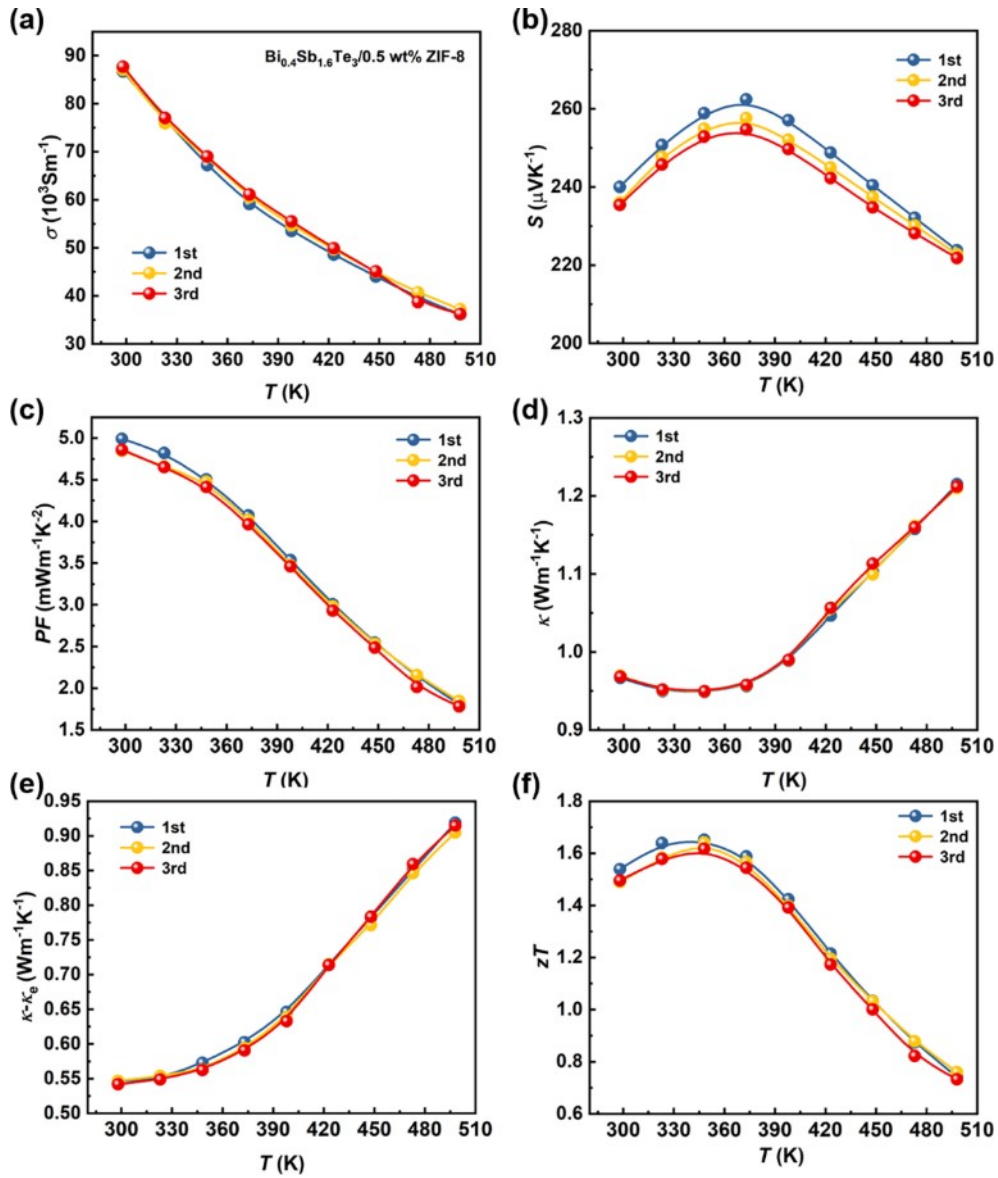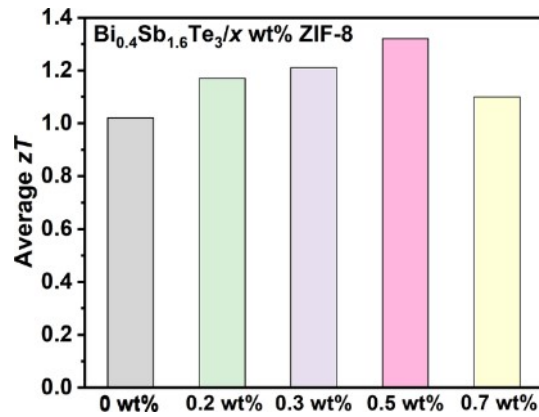**Fig. S27** The average zT (zT_{avg}) of $Bi_{0.4}Sb_{1.6}Te_3$/x wt% ZIF-8 (x = 0, 0.2, 0.3, 0.5, 0.7) samples measured in the direction vertical to SPS compressing.

Generality for Bi$_{0.4}$Sb$_{1.6}$Te$_3$ (BST) composite UiO-66
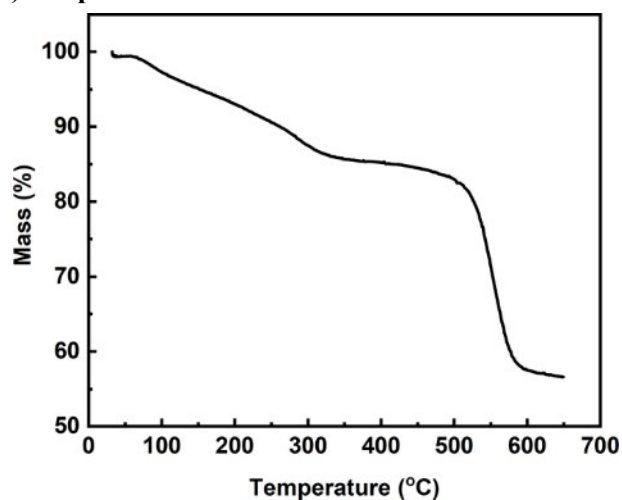
Fig. S28 TG curve for UiO-66 measured simultaneously in a flow of N$_2$. The initial weight-loss step, observed in the temperature range of 50-150 °C, is attributed to the desorption of water molecules. The second weight-loss step, observed in the temperature range of 150-350 °C, is related to the thermal desorption of DMF or the dehydroxylation of the Zr nodes ([Zr$_6$O$_4$(OH)$_4$]). The third weight loss step at 500 °C corresponds to the vaporization of the organic linker in the UiO-66 crystals.[8-10]
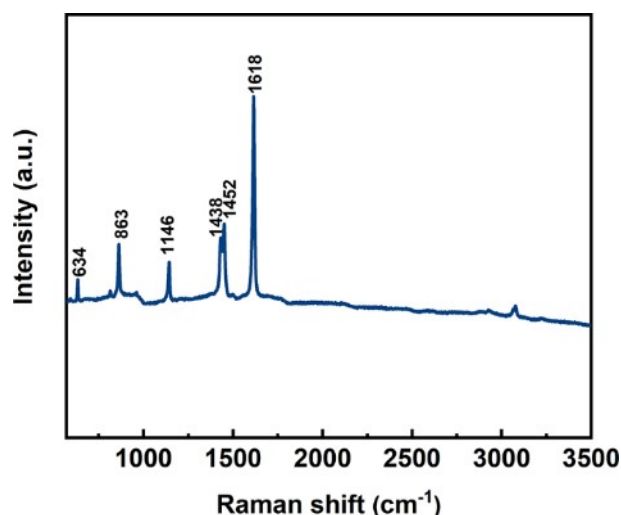
Fig. S29 Raman spectra of UiO-66 particles. The predominant Raman band at 1618 cm^{-1} is attributed to the C=C aromatic stretch in the BDC linker phase, while the vibrational signature of the aromatic ring in-plane bending is observed at 634 cm^{-1}. The doublet, peaking at 1452 and 1438 cm^{-1}, originates from the in-phase OCO symmetric stretching of the carboxylate group in the BDC linker.[11, 12]
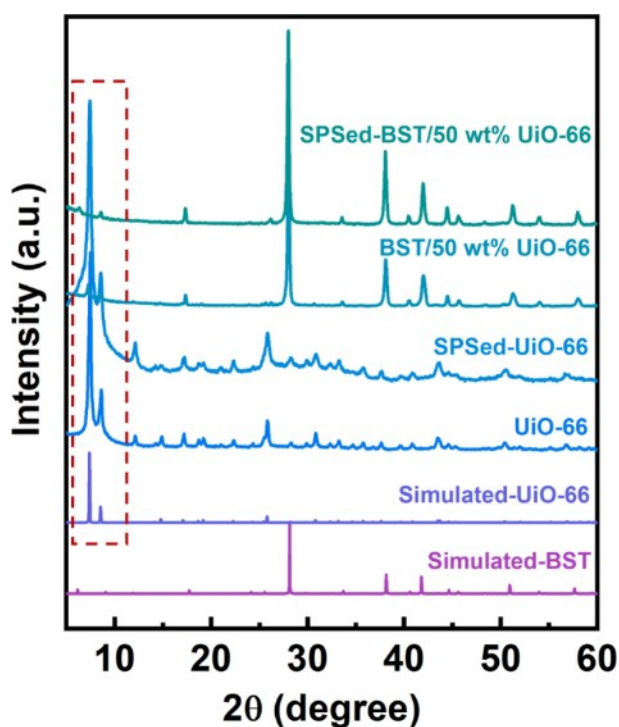
Fig. S30 XRD patterns of UiO-66, SPSed-UiO-66, BST/50 wt% UiO-66, and SPSed-BST/50 wt% UiO-66. For the as-prepared UiO-66 and SPSed-UiO-66, two prominent characteristic peaks at 2θ = 7.4° and 8.5° correspond to the (111) and (200) planes of UiO-66, respectively. These peaks align closely with simulated results, signifying no decomposition during the sintered process. After compounding with BST, the position of characteristic peaks remains unaltered, indicating the unchanged phase of UiO-66, except for a decrease in the intensity of the main peaks.
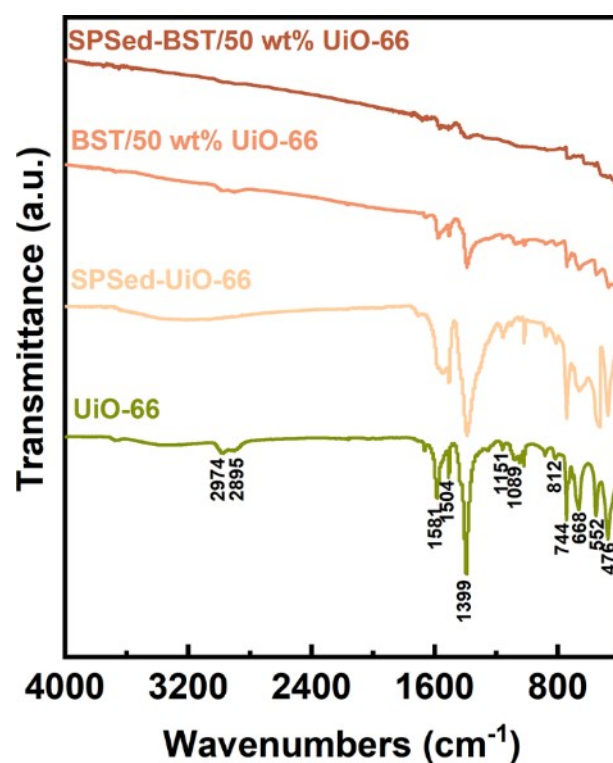
Fig. S31 FTIR spectrum of UiO-66, SPSed-UiO-66, BST/50 wt% UiO-66, and SPSed-BST/50 wt% UiO-66. The vibrational bands spanning from 2974 and 2895 cm^{-1} are indicative of C–H stretching. The bands at 1581 and 1399 cm^{-1} can be assigned to the asymmetric and symmetric stretching of v(OCO), respectively. The minor band at 1504 cm^{-1} signifies the characteristic vibration of the C=C bond in a benzene ring. The band at around 1100 cm^{-1} corresponds to the stretching vibration of the Zr−O single bond within the framework. Peaks at 812, 744, and 668 cm^{-1} arise from OH and C−H vibration in the terephthalic acid ligand. At lower frequencies, modes associated with OH and CH bending intermingle with Zr−O modes, with primary bands at 744, 668, 552, and 478 cm^{-1}. The vibration mode at 668 cm^{-1} can be ascribed to the μ_3-O stretching of the Zr$_6$O$_4$(OH)$_4$(−CO$_2$)$_{12}$ in the UiO-66 framework.[9, 10, 12]

Table S4. The density of the SPS sintered BST/UiO-66 nanocomposite.

Samples	BST	BST/0.2 wt% UiO-66	BST/0.3 wt% UiO-66	BST/0.5 wt% UiO-66	BST/0.7 wt% UiO-66
Density (g/cm³)	6.62	6.55	6.51	6.48	6.45
Relative Density	98.3%	97.2%	96.6%	96.2%	95.7%
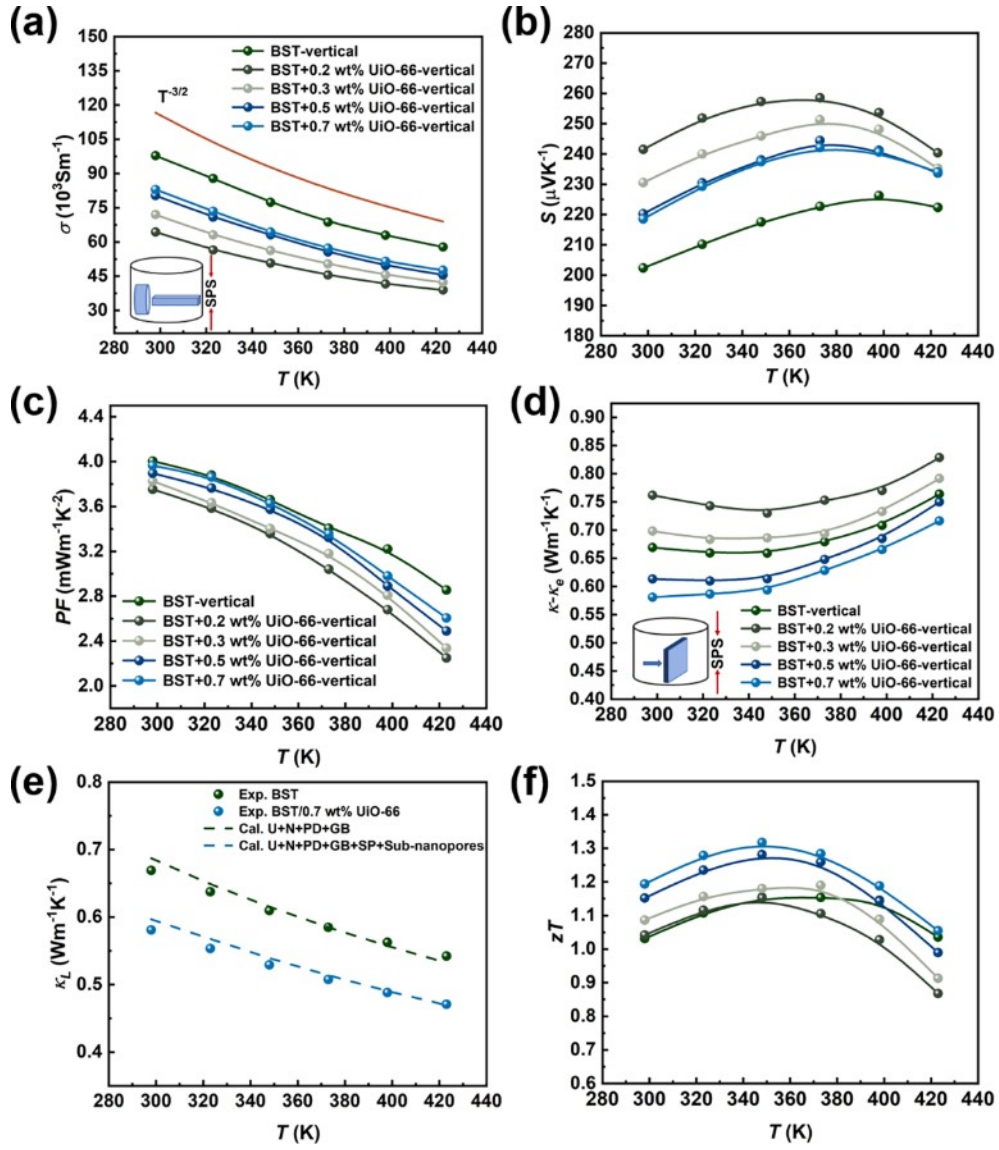
Fig. S32 Temperature-dependent thermoelectric properties of BST/x wt% UiO-66 samples measured in the direction vertical to SPS compressing. (a) Electrical conductivity σ. (b) Seebeck coefficient S. (c) Power factor PF. (d) κ_{tot}-κ_e term. (e) The measured and fitted lattice thermal conductivity κ_L. (f) Figure of merit zT.
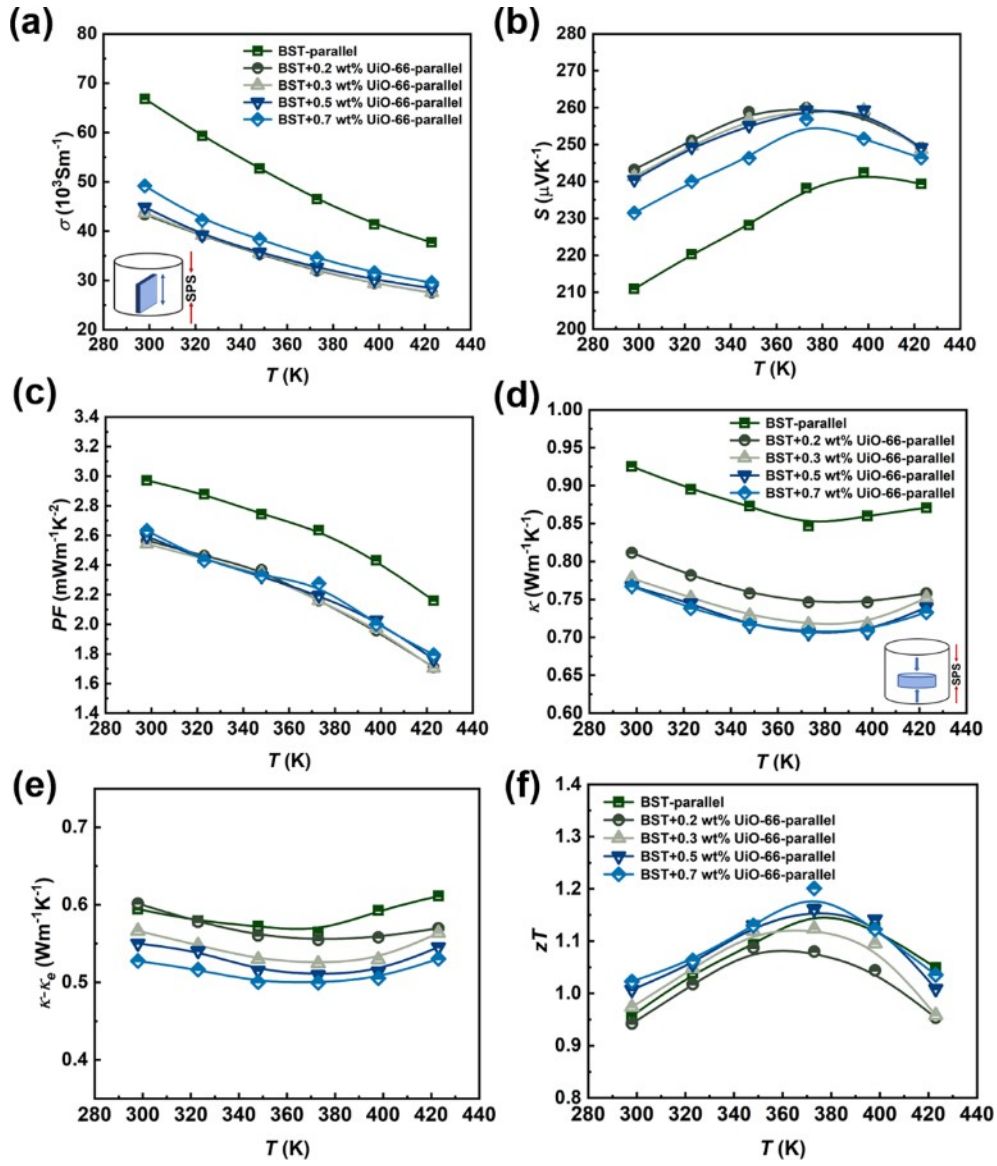
Fig. S33 Temperature-dependent thermoelectric properties of BST/x wt% UiO-66 samples measured in the direction parallel to SPS compressing. (a) Electrical conductivity σ. (b) Seebeck coefficient S. (c) Power factor PF. (d) Total thermal conductivity κ_{tot}. (e) κ_{tot}-κ_e term. (f) Figure of merit zT.

Generality for Bi$_{0.4}$Sb$_{1.6}$Te$_3$ (BST) composite MIL-101
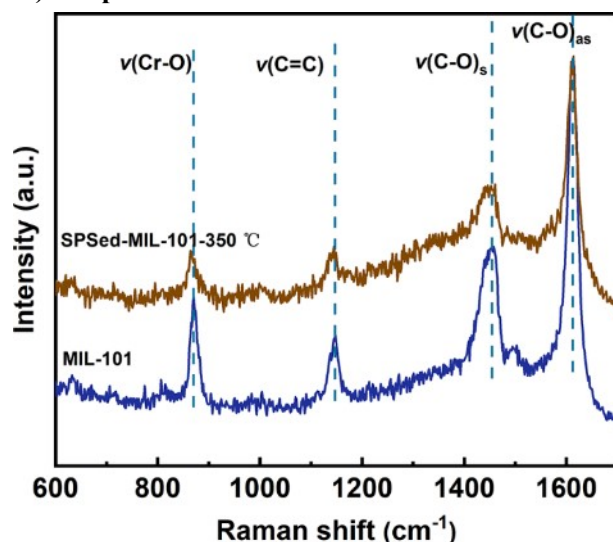
Fig. S34 Raman spectra of MIL-101 and SPSed-MIL-101-350 °C. The Raman results highlight the production of high-quality MIL-101 particles and the preservation of MIL-101 structure following SPS.[13]
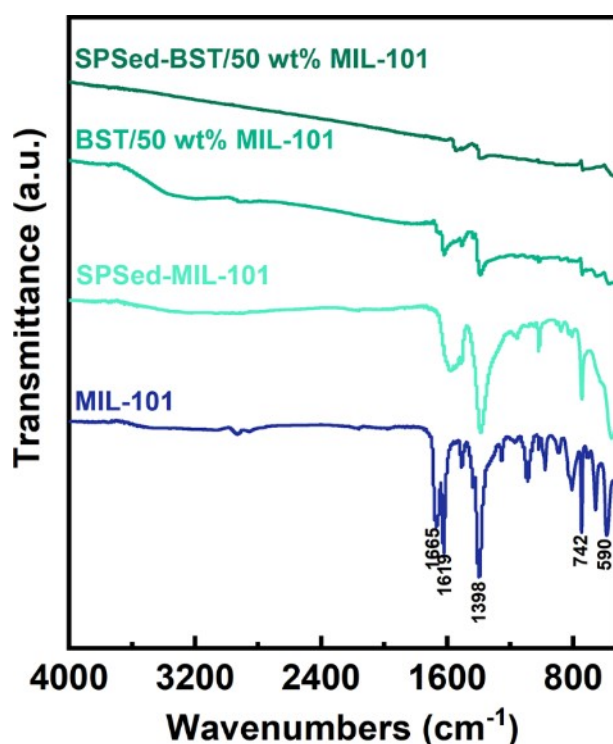
Fig. S35 FTIR spectrum of MIL-101, SPSed-MIL-101, BST/50 wt% MIL-101 and SPSed-BST/50 wt% MIL-101. The bands observed at 1619 and 1398 cm^{-1} are attributed to the O-C-O symmetric vibrations of dicarboxylate, providing evidence of the existence of H$_2$BDC in MIL-101. Additionally, the band at 590 cm^{-1} is assigned to the bending of modes of COO$^-$ groups.[14]

Table S5. The density of the SPS sintered BST/MIL-101 nanocomposite.

Samples	BST	BST/0.2 wt% MIL-101	BST/0.3 wt% MIL-101	BST/0.5 wt% MIL-101	BST/0.7 wt% MIL-101
Density (g/cm³)	6.58	6.55	6.51	6.45	6.38
Relative Density	97.7%	97.2%	96.6%	95.7%	94.7%
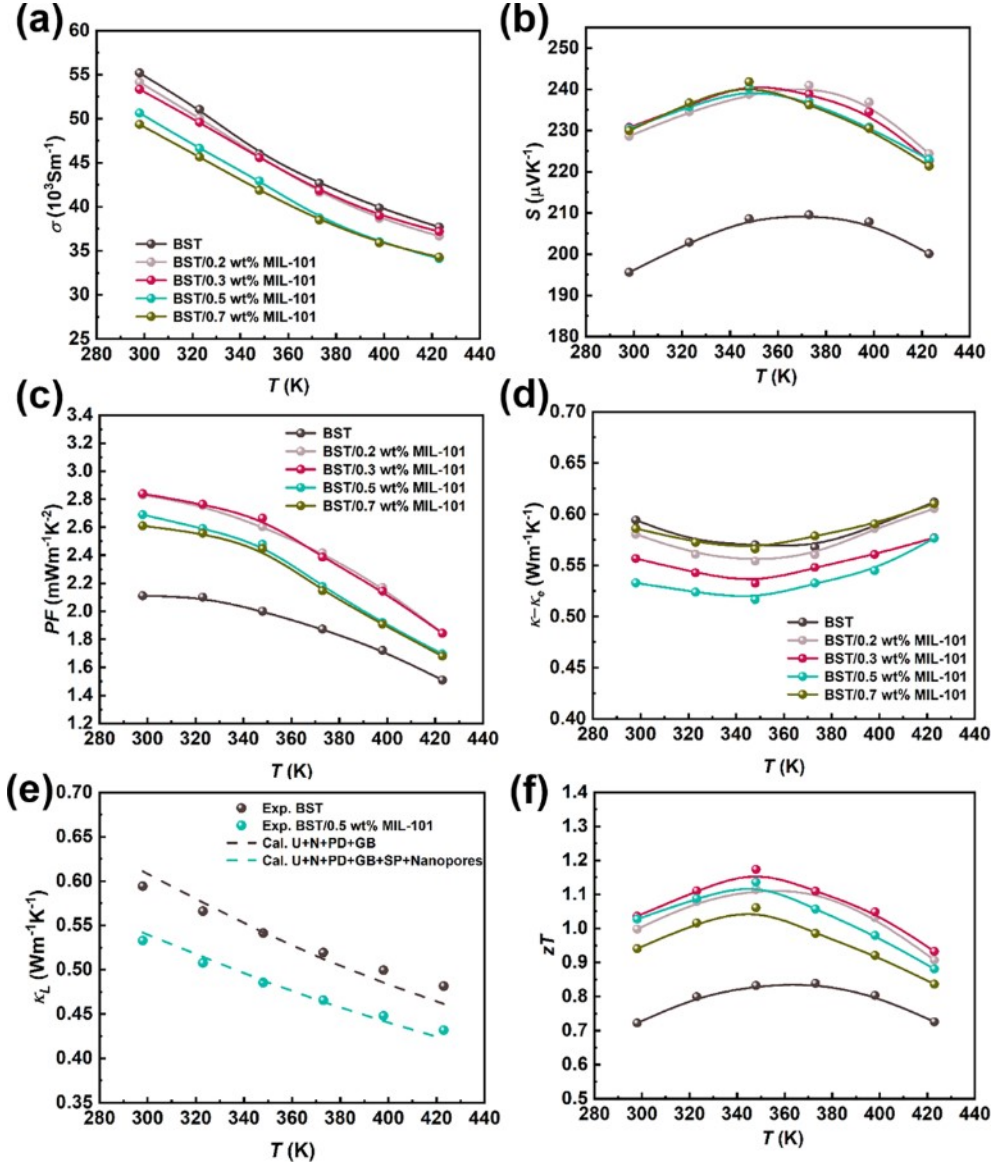
Fig. S36 Temperature-dependent thermoelectric properties of BST/*x* wt% MIL-101 samples. (a) Electrical conductivity σ. (b) Seebeck coefficient S. (c) Power factor PF. (d) κ_{tot}-κ_e term. (e) The measured and fitted lattice thermal conductivity κ_L. (f) Figure of merit zT.

Generality for $Bi_{0.4}Sb_{1.6}Te_3$ (BST) composite MOF-919
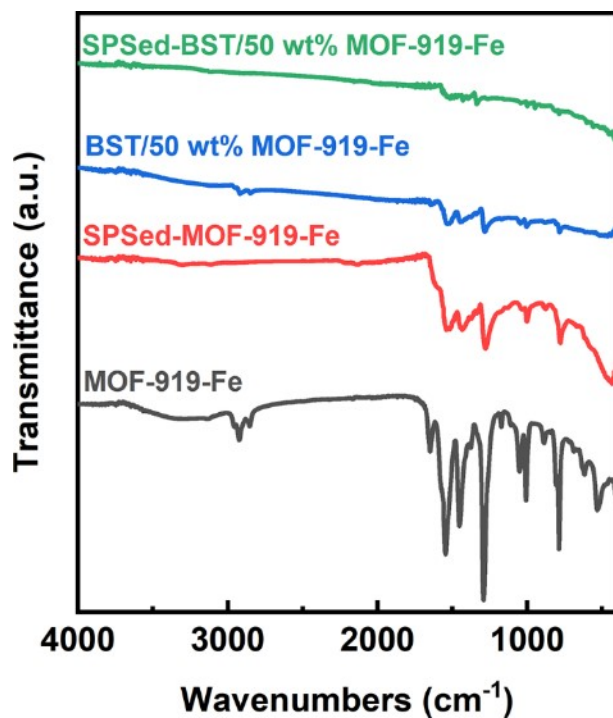
Fig. S37 FTIR spectrum of MOF-919-Fe, SPSed-MOF-919-Fe, BST/50 wt% MOF-919-Fe and SPSed-BST/50 wt% MOF-919-Fe. The primary peaks at 1652 cm^{-1}, 1448 cm^{-1}, and 1384 cm^{-1} are attributed to the stretching vibrations of C=C, C–C, and C–N, respectively. The peak at 1008 cm^{-1} is attributed to N–Cu–N vibrations, while the peak around 526 cm^{-1} corresponds with the Fe–O–Fe vibrational band.[15]

Table S6. The density of the SPS sintered BST/MOF-919 nanocomposite.

| Samples	BST	BST/0.2 wt% MOF-919	BST/0.5 wt% MOF-919	BST/0.7 wt% MOF-919
Density (g/cm³)	6.38	6.32	6.38	6.39
Relative Density	94.7%	93.8%	94.7%	94.8%
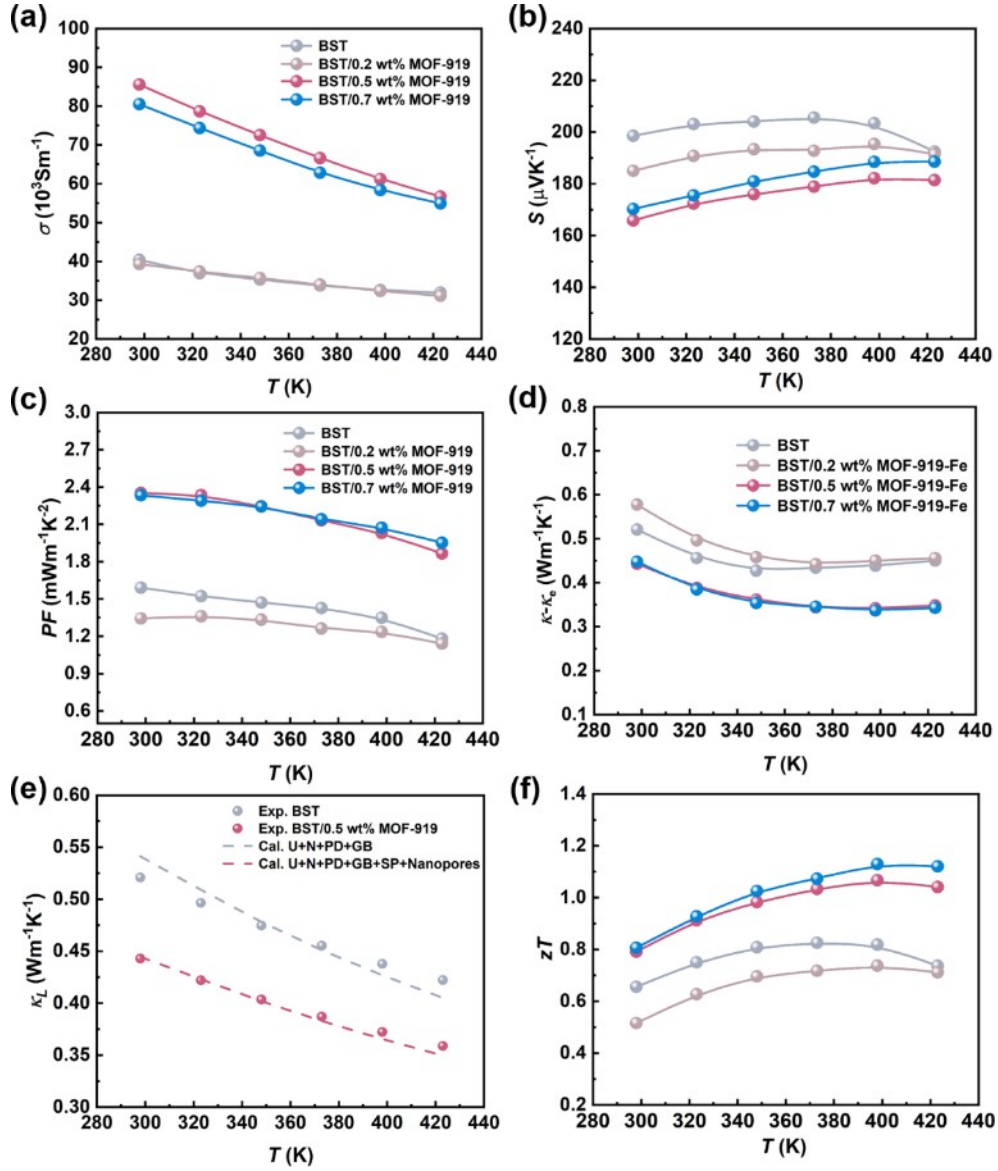
Fig. S38 Temperature-dependent thermoelectric properties of BST/x wt% MOF-919 samples. (a) Electrical conductivity σ. (b) Seebeck coefficient S. (c) Power factor PF. (d) κ_{tot}-κ_e term. (e) The measured and fitted lattice thermal conductivity κ_L. (f) Figure of merit zT.

Theoretical calculations

DFT calculation

The crystal structure of $Bi_{0.4}Sb_{1.6}Te_3$ with a space group of *R-3m:H* (166) was obtained from the Crystallography Open Database (No. 1530822). The projector-augmented wave[16] method and Perdew-Burke-Ernzerhof (PBE) exchange-correlation functional[17] were employed for Density-functional theory calculations.[18] The energy convergence precision of the whole calculation process is below 10^{-5} eV/atom, while the Hellman-Feynman force is smaller than -0.03Å/atom in the optimized supercell. The Γ-centered scheme was adopted for grid generation of all DFT computations.

The phonon density of states (PDOS) was calculated by using the Phonopy package. The exchange-correlation energy function is approximated by using local-density approximations (LDA). The plane-wave energy cutoff is set as 500 eV for both unit cell and supercell calculations. The unit cell is relaxed until the force is smaller than 10^{-6} eV/Å with an energy convergence threshold of 10^{-8} eV/Å.

Calculation of scattering parameter *r*

In general, *S* of a degenerate semiconductor can be expressed by the Mott equation:[19]

$$S = \frac{\pi^2 k_B^2 T}{3e}[\frac{1}{p}\frac{\partial n(E)}{\partial E} + \frac{1}{\mu}\frac{\partial \mu(E)}{\partial E}]_{E = E_f}$$

(S1)

where k_B, *e*, and E_f are the Boltzmann constant, carrier charge and Fermi energy, respectively.

Based on the assumption of the single parabolic band (SPB) model, *S* and *p* can be written as the following equations:[20]

$$S = \frac{k_B}{e}[\frac{(\frac{5}{2} + r)F_{r+\frac{3}{2}}(\eta)}{(\frac{3}{2} + r)F_{r+\frac{1}{2}}(\eta)} - \eta]$$

(S2)

$$p = \frac{4\pi(2m^* k_B T)^{\frac{3}{2}}}{h^3}F_{\frac{1}{2}}(\eta)$$

(S3)

With a Fermi integral order of *i*

$$F_i(\eta) = \int_0^\infty \frac{\chi^i}{1 + exp(\chi - \eta)}d\chi$$

(S4)

where m^*, h, $F_i(\eta)$ and η correspond to the effective mass, Planck constant, Fermi-Dirac integral and reduced Fermi level $E_f/(k_BT)$. The effective mass $m^* = 1.29\,m_0$ (where m_0 is the free electron mass) of the $Bi_{0.4}Sb_{1.6}Te_3$ matrix at 300 K was determined using the carrier concentration and the Seebeck coefficient, assuming the acoustic phonon scattering is the dominant carrier scattering mechanism ($r = -0.5$).[21] Since the addition of second phase is unlikely to alter the general band structure of BST matrix, m^* is treated as a constant at fixed temperature.[22, 23] Therefore, we assumed that m^* remains unchanged for different samples, and the r values of all samples were calculated with formula (S2) - (S4).

Model of lattice thermal conductivity

The Debye-Callaway model explains the total phonon relaxation time (τ_{tot}) as the reciprocal sum of individual relaxation times, presuming that acoustic phonons constitute the primary contribution to lattice thermal conductivity. The lattice thermal conductivity is described by the following equation:[24-29]

$$k_{lat} = \frac{k_B}{2\pi^2 v}(\frac{k_B T}{\hbar})\int_0^{\theta_D/T} \tau_{tot}(x)\frac{x^4 e^x}{(e^x - 1)^2}dx$$

(S5)

where k_B is the Boltzmann constant, $\hbar$ is the reduced Plank constant, x is $\hbar\omega/k_BT$ with a phonon angular frequency of ω, v is the average sound speed, θ_D is the Debye temperature, and τ_{tot} is the total phonon relaxation time. According to Matthiessen's rule, the total phonon relaxation time (τ_{tot}) is a reciprocal sum of the relaxation times. Umklapp phonon-phonon scattering, normal phonon-phonon scattering, grain boundary scattering, point defect scattering, second phase scattering and sub-nanopore scattering were considered:[27, 29]

$$\tau_{tot}^{-1} = \tau_U^{-1} + \tau_N^{-1} + \tau_{GB}^{-1} + \tau_{PD}^{-1} + \tau_{SP}^{-1} + \tau_{pore}^{-1}$$

(S6)

Spectral lattice thermal conductivity was also calculated for further understanding of the scattering mechanism:[25]

$$k_s = C_v(\omega) \cdot v^2(\omega) \cdot \tau(\omega)$$

(S7)

The contribution of Umklapp (τ_U^{-1}) and Normal (τ_N^{-1}) processes to the relaxation time can be expressed as:[28, 30]

$$\tau^{-1}_U + \tau^{-1}_N = A\frac{2k_B V^{1/3}\gamma^2\omega^2 T}{(6\pi^2)^{1/3}Mv^3}$$

(S8)

where A is a comprehensive coefficient, since τ^{-1}_U is in proportion to τ^{-1}_N, and 3.9 is used from the fitted data. V is the atomic volume of $Bi_{0.4}Sb_{1.6}Te_3$, γ is the Grüneisen parameter, T is the absolute temperature, and M is the atomic mass of the sample, respectively.

The contribution of grain boundary scattering to the relaxation time can be expressed as:[29]

$$\tau^{-1}_{GB} = \frac{v}{d}$$

(S9)

where d is the average grain size.

The point defect scattering in $Bi_{0.4}Sb_{1.6}Te_3$ is originated from the disordered arrangement of Bi and Sb atoms in the equivalent position, which can be expressed as:[31, 32]

$$\tau^{-1}_{PD} = \frac{V\omega^4}{4\pi v^3}\Gamma$$

(S10)

where Γ is point defect scattering parameter and the fitted value is 0.105.

When regarding the MOF and nanopores as a solid spherical second phase, the contribution of their scattering to the relaxation time can be expressed as:[27, 33]

$$\tau^{-1}_{SP} = v\left(\sigma^{-1}_s + \sigma^{-1}_l\right)V_S$$

(S11)

In this equation, σ_s and σ_l are the scattering cross-section in short- and long- wavelength regimes, respectively. Their expressions are as follows:

$$\sigma_s = 2\pi R^2$$

(S12)

$$\sigma_l = \frac{4}{9}\pi R^2\left(\frac{\Delta D}{D}\right)^2\left(\frac{R}{v}\omega\right)^4$$

(S13)

where R is the equivalent mean radius of the second phase, D and ΔD are the mass density of matrix and density difference between matrix and second phase (the mass density of pores is considered as 0), respectively; V_S is the number density of the second phase. All parameters involved above are given in the Table S7.

Table S7. Parameters for the calculation of lattice thermal conductivity.

Parameters	Notes	Values	Methods
v	Average speed of sound	2147 m s^{-1}	[29]
v_L	Longitudinal speed of sound	2884 m s^{-1}	[29]
v_T	Transverse speed of sound	1780 m s^{-1}	[29]
θ_D	Debye temperature	157 K	[34]
V	Average atomic volume of $Bi_{0.4}Sb_{1.6}Te_3$	3.18×10^{-29} m^3	[35]
M	Average atomic mass of $Bi_{0.4}Sb_{1.6}Te_3$	2.21×10^{-25} kg	[29]
γ	Grüneisen parameter	2.3	[36]
d	Grain size	973 nm	Experimental
Γ	Atomic size disorder scattering parameter	0.145	[29]
r	Poisson's ratio	0.24	[29]
R	Equivalent mean radius of the nanopores and MOF as second phases	0.44 nm, 80 nm (ZIF-8)	Experimental
		0.375 nm, 90 nm (UiO-66)	[37]
		0.725 nm, 100 nm (MIL-101)	[38]
		2 nm, 5 um (MOF-919)	[39]
D	Mass density	6.62 g cm^{-3} (BST)	Experimental
		1.141 g cm^{-3} (ZIF-8)	Calculated
		1 g cm^{-3} (UiO-66)	Calculated
		0.62 g cm^{-3} (MIL-101)	Calculated
		1.141 g cm^{-3} (MOF-919)	Calculated
	Number density of nanopores	1.23×10^{26} m^{-3} (ZIF-8)	-
	Number density of nanopores	8.22×10^{24} m^{-3} (UiO-66)	-

	Number density of nanopores	1.36×10^{26} m^{-3} (MIL-101)	-
	Number density of nanopores	1.44×10^{26} m^{-3} (MOF-919)	-
V_s	Number density of MOF	8.07×10^{19} m^{-3} (ZIF-8)	-
	Number density of MOF	9.35×10^{19} m^{-3} (UiO-66)	-
	Number density of MOF	8.81×10^{19} m^{-3} (MIL-101)	-
	Number density of MOF	8.58×10^{19} m^{-3} (MOF-919)	-

Calculation of interface thermal resistance R_k

To quantify the effect of ZIF-8 nanoparticles on suppressing k_L, we calculated the R_k via a phenomenological model:[40-42]

The lattice thermal conductivity in a polycrystalline BST could be expressed as:

$$k_{poly}^{-1} = k_{bulk}^{-1} + R_k/l \qquad (S14)$$

in which κ_{bulk} is the intrinsic thermal conductivity in a single crystal (the κ_{bulk} of BST single crystal was found to be 0.82 W m^{-1} K^{-1}),[43] l is the average grain size of polycrystalline (the average grain size of the pristine BST and BST/0.5 wt% ZIF-8 are about 973 nm obtained from the SEM results) and R_κ is the interface resistance.

Similarly, the corresponding interfacial thermal resistance of nanocomposite can be calculated by:

$$k_{comp}^{-1} = k_{poly}^{-1} + R_k^{'}/l \qquad (S15)$$

References for Supporting Information

1. O. Kolmykov, J.-M. Commenge, H. Alem, E. Girot, K. Mozet, G. Medjahdi and R. Schneider, *Mater. Des.*, 2017, **122**, 31-41.

2. N. Missaoui, H. Kahri and U. B. Demirci, *J. Mater. Sci.*, 2022, **57**, 16245-16257.

3. J. Yao, R. Chen, K. Wang and H. Wang, *Microporous Mesoporous Mater.*, 2013, **165**, 200-204.

4. P. D. Du, N. T. Hieu and T. V. Thien, *J. Nanomater.*, 2021, **2021**, 1-12.

5. Y. Wang, X. Dai, Y. Zhan, X. Ding, M. Wang and X. Wang, *Int. J. Biol. Macromol.*, 2019, **137**, 77-86.

6. X. Yang, T. Song, T. Su, J. Hu and S. Wu, *Processes*, 2022, **10**, 1705.

7. J. Chen, M. Zhang, S. Zhang, K. Cao, X. Mao, M. Zhang, L. He, X. Dong, J. Shu, H. Dong, F. Zhai, R. Shen, M. Yuan, X. Zhao, G. Wu, Z. Chai and S. Wang, *Angew. Chem., Int. Ed.*, 2022, **61**, e202212532.

8. J. Winarta, B. Shan, S. M. McIntyre, L. Ye, C. Wang, J. Liu and B. Mu, *Cryst. Growth Des.*, 2020, **20**, 1347-1362.

9. E. Geravand, F. Farzaneh and M. Ghiasi, *J. Mol. Struct.*, 2019, **1198**, 126940.

10. H. N. Abdelhamid, *Dalton Trans.*, 2020, **49**, 10851-10857.

11. X. Chang, X.-F. Yang, Y. Qiao, S. Wang, M.-H. Zhang, J. Xu, D.-H. Wang and X.-H. Bu, *Small*, 2020, **16**, 1906432.

12. C. Atzori, G. C. Shearer, L. Maschio, B. Civalleri, F. Bonino, C. Lamberti, S. Svelle, K. P. Lillerud and S. Bordiga, *J. Phys. Chem. C*, 2017, **121**, 9312-9324.

13. E. Gkaniatsou, R. Ricoux, K. Kariyawasam, I. Stenger, B. Fan, N. Ayoub, S. Salas, G. Patriarche, C. Serre, J.-P. Mahy, N. Steunou and C. Sicard, *ACS Appl. Nano Mater.*, 2020, **3**, 3233-3243.

14. L. Zhang, J. Qiu, D. Dai, Y. Zhou, X. Liu and J. Yao, *J. Cleaner Prod.*, 2022, **341**, 130891.

15. Q. Liu, Y. Song, Y. Ma, Y. Zhou, H. Cong, C. Wang, J. Wu, G. Hu, M. O'Keeffe and H. Deng, *J. Am. Chem. Soc.*, 2019, **141**, 488-496.

16. P. Blochl, E. Blöchl, P. Blöchl, *Phys. Rev. B: Condens Matter*. 1994, **50**, 17953-17979.

17. J. P. Perdew, K. Burke, M. Ernzerhof, *Phys. Rev. Lett.* 1996, **77**, 3865.

18. E. J. Baerends, *Theor. Chem. Acc.*, 2000, **103**, 265-269.

19. Y. Li, D. Li, X. Qin, X. Yang, Y. Liu, J. Zhang, Y. Dou, C. Song and H. Xin, *J. Mater. Chem. C*, 2015, **3**, 7045-7052.

20. W. H. Shin, J. W. Roh, B. Ryu, H. J. Chang, H. S. Kim, S. Lee, W. S. Seo and K. Ahn, *ACS Appl. Mater. Interfaces*, 2018, **10**, 3689-3698.

21. A. F. May, E. S. Toberer, A. Saramat and G. J. Snyder, *Phys. Rev. B*, 2009, **80**, 125205.

22. G. J. Snyder and E. S. Toberer, *Nat. Mater.*, 2008, **7**, 105-114.

23. S. Sumithra, N. J. Takas, D. K. Misra, W. M. Nolting, P. F. P. Poudeu and K. L. Stokes, *Adv. Energy Mater.*, 2011, **1**, 1141-1147.

24. Y. Pan, U. Aydemir, J. A. Grovogui, I. T. Witting, R. Hanus, Y. Xu, J. Wu, C.-F. Wu, F.-H. Sun, H.-L. Zhuang, J.-F. Dong, J.-F. Li, V. P. Dravid and G. J. Snyder, *Adv. Mater.*, 2018, **30**, 1802016.

25. J. Callaway and H. C. von Baeyer, *Phys. Rev.*, 1960, **120**, 1149-1154.

26. F.-H. Sun, J. Dong, H. Tang, P.-P. Shang, H.-L. Zhuang, H. Hu, C.-F. Wu, Y. Pan and J.-F. Li, *Nano Energy*, 2019, **57**, 835-841.

27. D. Wu, L.-D. Zhao, F. Zheng, L. Jin, M. G. Kanatzidis and J. He, *Adv. Mater.*, 2016, **28**, 2737-2743.

28. Y. Yu, D.-S. He, S. Zhang, O. Cojocaru-Mirédin, T. Schwarz, A. Stoffers, X.-Y. Wang, S. Zheng, B. Zhu, C. Scheu, D. Wu, J.-Q. He, M. Wuttig, Z.-Y. Huang and F.-Q. Zu, *Nano Energy*, 2017, **37**, 203-213.

29. S. I. Kim, K. H. Lee, H. A. Mun, H. S. Kim, S. W. Hwang, J. W. Roh, D. J. Yang, W. H. Shin, X. S. Li, Y. H. Lee, G. J. Snyder and S. W. Kim, *Science*, 2015, **348**, 109-114.

30. E. S. Toberer, A. Zevalkink and G. J. Snyder, *J. Mater. Chem.*, 2011, **21**, 15843-15852.

31. H. Wang, A. D. LaLonde, Y. Pei and G. J. Snyder, *Adv. Funct. Mater.*, 2013, **23**, 1586-1596.

32. D. T. Morelli, J. P. Heremans and G. A. Slack, *Phys. Rev. B*, 2002, **66**, 195304.

33. W. Kim and A. Majumdar, *J. Appl. Phys.*, 2006, **99**, 084306.

34. D. Bessas, I. Sergueev, H. C. Wille, J. Perßon, D. Ebling and R. P. Hermann, *Phys. Rev. B*, 2012, **86**, 224301.

35. S. Lee, S.-J. Jung, G. M. Park, M. Y. Na, K.-C. Kim, J. Hong, A. S. Lee, S.-H. Baek, H. Kim, T. J. Park, J.-S. Kim and S. K. Kim, *Small*, 2023, **19**, 2205202.

36. X. Chen, H. D. Zhou, A. Kiswandhi, I. Miotkowski, Y. P. Chen, P. A. Sharma, A. L. Lima Sharma, M. A. Hekmaty, D. Smirnov and Z. Jiang, *Appl. Phys. Lett.*, 2011, **99**, 261912.

37. D. Jiang, A. D. Burrows and K. J. Edler, *CrystEngComm*, 2011, **13**, 6916-6919.

38. J. H. Cavka, S. Jakobsen, U. Olsbye, N. Guillou, C. Lamberti, S. Bordiga and K. P. Lillerud, *J. Am. Chem. Soc.*, 2008, **130**, 13850-13851.

39. Q. Liu, Y. Song, Y. Ma, Y. Zhou, H. Cong, C. Wang, J. Wu, G. Hu, M. O'Keeffe and H. Deng, *J. Am. Chem. Soc.*, 2019, **141**, 488-496.

40. P.-a. Zong, R. Hanus, M. Dylla, Y. Tang, J. Liao, Q. Zhang, G. J. Snyder and L. Chen, *Energy Environ. Sci.*, 2017, **10**, 183-191.

41. Q. Zhang, Z. Zhou, M. Dylla, M. T. Agne, Y. Pei, L. Wang, Y. Tang, J. Liao, J. Li, S. Bai, W. Jiang, L. Chen and G. Jeffrey Snyder, *Nano Energy*, 2017, **41**, 501-510.

42. X. Hu, K. Nagase, P. Jood, M. Ohta and A. Yamamoto, *J. Electron. Mater.*, 2015, **44**, 1785-1790.

43. Q. Jiang, H. Yan, J. Khaliq, H. Ning, S. Grasso, K. Simpson and M. J. Reece, *J. Mater. Chem. A*, 2014, **2**, 5785-5790.